A&A, 706, A95 (2026)
https://doi.org/10.1051/0004-6361/202555751

Astronomy & Astrophysics

The PHANGS-MUSE/HST-Hα nebulae catalogue

Parsec-scale resolved structure, physical conditions, and stellar associations across nearby galaxies

A. T. Barnes[1,⋆], R. Chandar[2], K. Kreckel[4], F. Belfiore[5], D. Pathak[8,9], D. Thilker[3], A. K. Leroy[8,9], B. Groves[6], S. C. O. Glover[7], R. McClain[8,9], A. Amiri[23], Z. Bazzi[18], M. Boquien[20], E. Congiu[14], D. A. Dale[13], O. V. Egorov[4], E. Emsellem[1,19], K. Grasha[11], J. Gonzalez Lobos[24], K. Henny[13], H. He[18], R. Indebetouw[21,22], J. C. Lee[10,26,27], J. Li[4], F.-H. Liang[4], K. Larson[10], D. Maschmann[26], S. E. Meidt[17], J. Eduardo Méndez-Delgado[15], J. Neumann[24], H.-A. Pan[25], M. Querejeta[16], E. Rosolowsky[28], S. K. Sarbadhicary[3], F. Scheuermann[4], L. Úbeda[10], T. G. Williams[12], T. D. Weinbeck[13], B. Whitmore[10], A. Wofford[19], and the PHANGS Collaboration

(Affiliations can be found after the references)

Received 30 May 2025 / Accepted 1 October 2025

ABSTRACT

We present the PHANGS-MUSE/HST-Hα nebulae catalogue, comprising 5177 spatially resolved nebulae across 19 nearby star-forming galaxies ($D < 20$ Mpc), based on high-resolution Hα imaging from HST, homogenised to a fixed (10 pc) physical resolution and sensitivity. Combined with MUSE integral field spectroscopy, this enables robust classification of 4882 H II regions and the separation of planetary nebulae and supernova remnants. We derive electron densities for 2544 H II regions using [S II] diagnostics and adopt direct or representative electron temperatures for consistent physical characterisation. Nebular sizes are measured using circularised radii and intensity-weighted second moments, yielding a median radius of approximately 20 pc and extending down to (sub-)parsec (deconvolved) radii. A structural complexity score is introduced via hierarchical segmentation to trace substructure, highlighting that around a third of the regions are H II complexes containing several individual clusters and bubbles, with an increased fraction of these regions in galactic centres. A luminosity–size relation, calibrated using the resolved HST sample, is applied to 30 790 MUSE nebulae, allowing the recovery of nebular sizes down to ∼1 pc and providing statistical completeness beyond the HST detection limit. Comparisons with classical Strömgren radii indicate that observed sizes are systematically larger, corresponding to typical volume filling factors with a median of $\epsilon \sim 0.22$ (10th–90th percentile 0.06–0.78), with larger regions exhibiting progressively lower values. We associate 3349 H II regions with stellar populations from the PHANGS-HST association catalogue, finding median ages of ∼3 Myr and typical stellar masses of around 10^4–10^5 $M_\odot$, supporting the link between ionised nebular and young stellar populations. We also assess the impact of diffuse ionised gas on emission-line diagnostics and after removing confirmed supernova remnants, find no strong variation in line ratios with nebular resolution, indicating minimal systematic bias in the MUSE catalogue. This dataset establishes a detailed, spatially resolved connection between nebular structure and ionising sources, and provides a benchmark for future studies of feedback, DIG contributions, and star formation regulation in the ISM, especially in combination with matched high-resolution observations. The full catalogue is made publicly available in machine-readable format.

Key words. HII regions – ISM: structure – galaxies: star clusters: general – galaxies: star formation

1. Introduction

Emission lines from ionised gas play a central role in our understanding of galaxy evolution over cosmic time (see the review by Kewley et al. 2019). These lines enable the determination of spectroscopic redshifts and provide critical diagnostics of key physical properties of galaxies, including star formation rates, the presence of active galactic nuclei (AGN), ionised gas kinematics, gas-phase metallicities, extinction, and more (e.g. Baldwin et al. 1981; Kewley et al. 2001; Sánchez et al. 2024). Past and ongoing observational surveys have leveraged advances in instrumentation – such as long-slit spectral stepping (e.g. the TYPHOON survey; Ho et al. 2017; Grasha et al. 2022), imaging Fourier transform spectrographs (e.g. SIGNALS with SITELLE on the CFHT; Rousseau-Nepton et al. 2019), and integral field spectroscopy (IFS; e.g. CALIFA, MaNGA, SAMI, and SDSS V LVM (Sánchez et al. 2012; Bundy et al. 2015; Bryant et al. 2015; Drory et al. 2024), as well as MAD, TIMER, PHANGS, and GECKOS with MUSE/VLT; Erroz-Ferrer et al. 2019; Gadotti et al. 2019; Emsellem et al. 2022; van de Sande et al. 2024) – to map multiple emission lines across thousands of galaxies.

However, the individual ionised nebulae responsible for these emission lines, such as H II regions, planetary nebulae, supernova remnants, and the narrow and broad-line regions of AGN, are typically much smaller than the ∼100 pc spatial resolution achievable in ground-based surveys of galaxies out to only a few Mpc (e.g. Schinnerer & Leroy 2024). Fully spatially resolved studies of individual nebulae are therefore largely confined to the

⋆ Corresponding author: ashley.barnes@eso.org

nearest systems, where ground-based observations can achieve physical resolutions of ~10 pc or better (e.g. Relaño & Kennicutt 2009; Lopez et al. 2011, 2014; McLeod et al. 2020; Della Bruna et al. 2020; Drory et al. 2024; Kreckel et al. 2024). This resolution gap limits the statistical power available to study the physical properties of nebulae across large samples of galaxy environments. In particular, it hinders the ability to determine the true physical extents of nebulae, characterise their internal morphology, disentangle overlapping structures, and distinguish compact sources from the surrounding diffuse ionised gas (DIG; e.g. Reynolds 1990; Haffner et al. 2009), introducing systematic uncertainties in efforts to study the physical conditions within nebulae and the impact of stellar feedback on the interstellar medium (ISM; see e.g. Barnes et al. 2021, 2022; Pathak et al. 2025).

In this work, we combine newly obtained Hα narrow-band imaging from the PHANGS-HST survey (Chandar et al. 2025), with physical resolutions of a few parsecs to 10 pc (for galaxy distances between 5 and 20 Mpc), and complementary MUSE integral field spectroscopy from the PHANGS-MUSE survey (Emsellem et al. 2022), with physical resolutions between a few tens to 100 pc. In synergy, the HST Hα narrow-band imaging enables detailed measurements of the resolved size, shape, and internal structure of each nebula, while the MUSE data provide key (previously unresolved) physical properties such as extinction, density, and ionisation state. Additionally, we incorporate broadband HST observations from the PHANGS-HST stellar association catalogue (Larson et al. 2023), which allow us to identify the embedded stellar populations powering each nebula. This unique combination connects the resolved morphology of the ionised gas with both its physical state and its stellar energy sources, enabling a complete view of the energy and momentum budget driving the evolution of each region.

This work presents a catalogue of over 5000 resolved nebulae across a representative sample of nearby star-forming galaxies – the largest to date to combine morphological, spectroscopic, and stellar population information at parsec-scale resolution. Quantifying nebular sizes and morphologies provides new constraints on feedback-regulated star formation, including porosity and filling factors (Sect. 5.2), the diffuse ionised background (Sect. 5.4), and enables tests of feedback-driven expansion (bubble growth, e.g. Watkins et al. 2023b,a). The resolved morphologies also allow direct comparison with bubble structures traced by mid-IR PAH emission in JWST observations, linking ionised gas to photodissociation regions at bubble interfaces (e.g. Barnes et al. 2023). Looking ahead, the catalogue provides an essential reference point for multi-wavelength studies: JWST (e.g. see right panel of Fig. 1) and ALMA data will extend these analyses into the embedded and molecular phases of star formation, while radio and near-IR tracers (e.g. Paα, Brα; Pedrini et al. 2024) provide dust-penetrating views of ionised gas. More broadly, the catalogue establishes a uniform, statistically powerful baseline against which detailed follow-up studies and theoretical models can be compared, offering a starting point for testing star formation efficiency, clustered feedback, and ISM regulation on galactic scales.

This paper is structured as follows. Section 2 describes the PHANGS-MUSE sample and the new PHANGS-HST Hα observations. Section 3 details the construction of the PHANGS-MUSE/HST-Hα nebulae catalogue, including source identification, measurement of physical and morphological properties, and association matching. An example of the final catalogue is presented in Appendix A, where we also provide a description of the delivered data products. The complete catalogue is available online via CDS, together with associated masks and maps, alongside a table documenting all columns. Section 4 presents the resulting population statistics, compares HST- and MUSE-based measurements, and places our results in context with prior studies. Section 6 summarises the main findings and outlines future directions.

2. Observations

This work primarily leverages observations taken as part of the PHANGS survey, which was designed specifically to resolve galaxies into individual elements of the star-formation process: molecular clouds, H II regions, and stellar clusters (see survey papers Leroy et al. 2021; Lee et al. 2022, 2023; Emsellem et al. 2022; Chandar et al. 2025; and also Figs. 1 and 2).

2.1. PHANGS-MUSE

In this work, we focus on the 19 nearby star-forming galaxies spectroscopically mapped as part of the PHANGS–MUSE survey (see Emsellem et al. 2022). This sub-sample of PHANGS galaxies spans a broad range of massive ($9.4 < \log M < 10.8$) spiral galaxies that lie along the main sequence of star-forming galaxies. These MUSE observations have a wavelength coverage of 4800 to 9300 Å, and achieved an average angular resolution of around 1″ (or around 50 pc at 10 Mpc). Further details on the sample, observations, reduction, and MUSE data products are provided in Emsellem et al. (2022).

2.2. The PHANGS-MUSE nebular catalogue

We use the PHANGS-MUSE nebular catalogue (Santoro et al. 2022; Groves et al. 2023), with updated auroral line fits (and associated properties) from Brazzini et al. (2024)[1]. The catalogue inherits the typical ~1 arcsec angular resolution of the MUSE observations Sect. 2.1), which sets the effective spatial resolution for all nebular measurements. This resolution enables the detection of thousands of distinct ionised nebulae across the 19 galaxies in the PHANGS-MUSE sample, but with the limitation of still blending compact substructures (see Sect. 2.3).

The PHANGS-MUSE nebular catalogue was produced using a modified version of the HIIPHOT algorithm (Thilker et al. 2000), as initially adapted by Kreckel et al. (2019) for application within the PHANGS-MUSE survey. The HIIPHOT algorithm functions by identifying significant, isolated peaks in the Hα emission map. These peaks represent potential nebulae, allowing the algorithm to systematically detect local maxima that are sufficiently spatially separated to be considered distinct structures. This method minimises the inclusion of diffuse emission and overlapping regions, effectively isolating nebulae. For each detected peak, the algorithm also defines spatial boundaries based on the Hα intensity contours, segmenting each nebula from the surrounding interstellar medium and nearby structures.

Across the full sample of 19 MUSE galaxies, Groves et al. (2023) identified 30 790 distinct nebulae as independent peaks in Hα emission. Note that the MUSE coverage and HST coverage do not exactly match (see Fig. 1), such that the total number of nebulae from the MUSE catalogue included within the HST Hα coverage (see Sect. 2.3) is 25 910 (~80%; see Table 1). These numbers exclude sources whose footprint falls within the (foreground) star masks, and also nebulae with centres within 1 PSF

[1] Also see the catalogues produced using the same PHANGS-MUSE observations but via an independent method by Congiu et al. (2023).

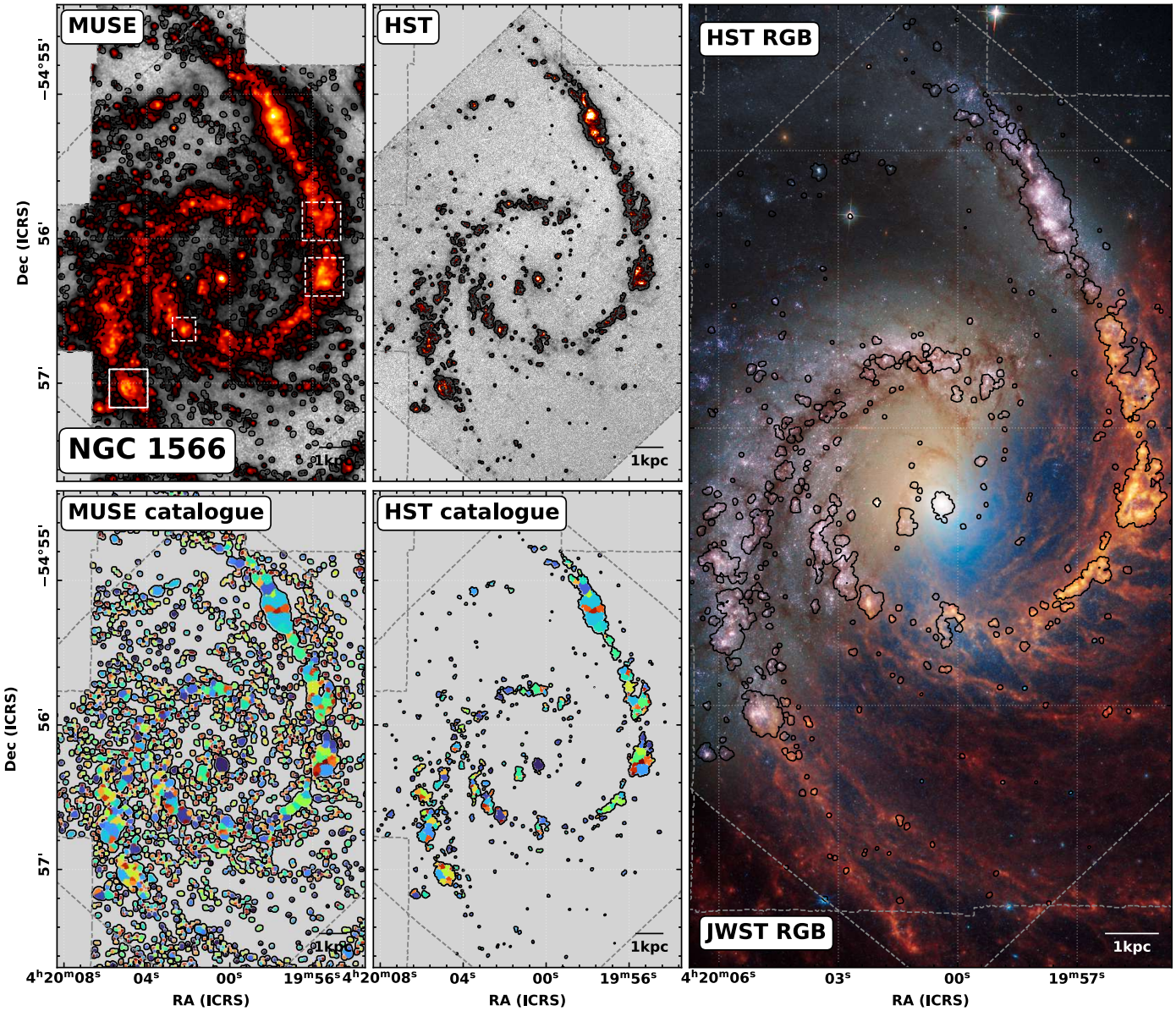

Fig. 1. Overview of the nebula catalogues towards NGC 1566. (*Upper left*) The background colour scale shows the Hα emission from the PHANGS-MUSE observations (Emsellem et al. 2022), overlaid with contours showing the boundaries of the sources identified in the PHANGS-MUSE Nebula Catalogue (Groves et al. 2023, see also Santoro et al. 2022). White boxes indicate the positions of the regions shown in Figs. 2 (solid lines) and C.1 (dashed lines). (*Upper centre*) The background colour scale shows the Hα emission from the PHANGS-HST Hα observations (Chandar et al. 2025), overlaid with contours showing the boundaries of the sources identified in this work in the PHANGS-HST Nebula Catalogue. (*Bottom left*) The PHANGS-MUSE Nebula Catalogue masks and (*bottom centre*) PHANGS-HST Nebula Catalogue masks are shown with the same colour scale, where the colours denote the region ID. (*Right*) Composite of separate exposures acquired with JWST using the NIRCam and MIRI instruments (Lee et al. 2023; Williams et al. 2024), and the HST using the ACS/WFC instrument (Lee et al. 2022). For the JWST part of the image, the assigned colours are Red = F2100W + F1130W + F1000W + F770W, Green = F770W + F360M, Blue = F335M + F300M. For the HST part of the image, the assigned colours are Red = F814W + F656N, Green = F555W, Blue = F435W. Overlaid as contours is the PHANGS-HST Nebula Catalogue (as in the other panels).

FWHM of the edges of the PHANGS–MUSE galaxy footprints (see Groves et al. 2023).

A radius is determined for each nebula from the circularised enclosed area, $r_{\rm circ} = \sqrt{A/\pi}$, where A is the area from Groves et al. (2023), calculated using the distances in Table B.1. The integrated MUSE spectra provided flux measurements for key emission lines, including Hα, Hβ, [O III], and [N II]. The dust extinction was measured using the Balmer decrement, and strong-line prescriptions were applied to derive gas-phase metallicities and ionisation parameters (see Groves et al. 2023 for details). Moreover, Groves et al. (2023) distinguished between the H II region population and other nebulae (e.g. planetary nebulae or supernova remnants) using the BPT (Baldwin et al. 1981) classification criteria from Kewley et al. (2001) and Kauffmann et al. (2003). There are 19 528 nebulae classified as H II regions out of the 25 910 nebulae within the catalogue covered by the HST observations. Lastly, Groves et al. (2023) also categorised nebulae based on their galactic environment (centre, bar, arm, inter-arm, and disc) using the environmental masks produced by Querejeta et al. (2021).

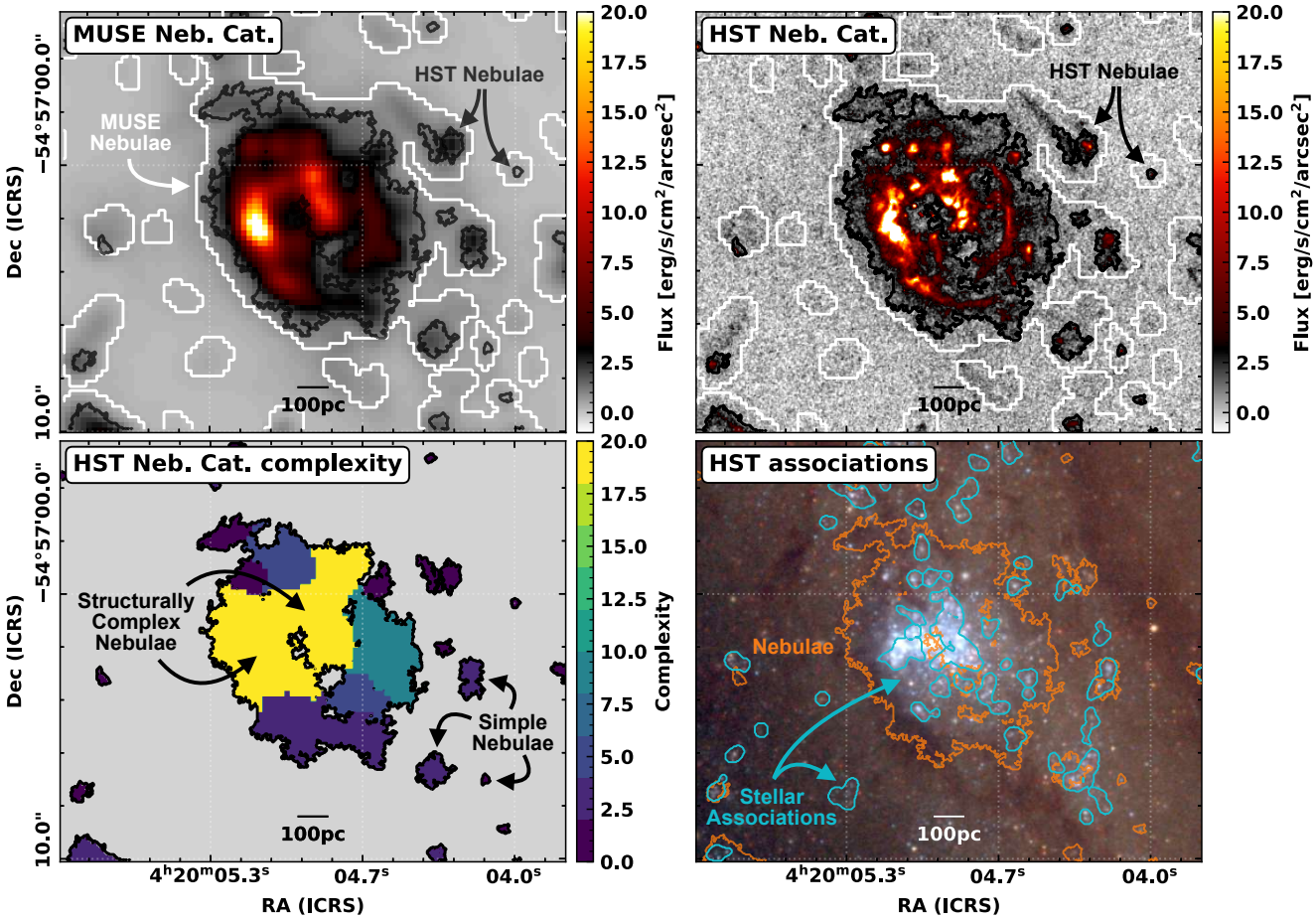

Fig. 2. Example of a H II complex region in NGC 1566 (see Sect. 3.4). (*Upper left panel*) MUSE observations and (*upper right*) HST Hα observations that are smoothed to a physical scale of 10 pc and with a fixed noise level (see Sect. 3.1). Each of these are overlaid with contours showing the boundary of the sources identified in the MUSE (white) and HST (black) observations. (*Lower left panel*) A map of the complexity score for the region (see Sect. 4.1). (*Lower right panel*) We show the nebula (orange contours) and 32 pc NUV-identified association (Larson et al. 2023; cyan contour) overlaid on a HST filter red (F814W) green (F555W) blue (F438W+F336W) image (see Lee et al. 2022). See Fig. C.1 for additional examples of simple, intermediate and complex nebulae within NGC 1566.

2.3. PHANGS-HST-Hα

The 19 galaxies in our sample (see Table B.1) were observed with high-angular-resolution Hα narrow-band imaging as part of the PHANGS-HST Treasury programme (PID 17126; PI Chandar) and a complementary General Observer programme (PID 17457; PI Belfiore). Full details of the observations, data reduction, and final products are given in Chandar et al. (2025); here we provide a brief summary.

For each galaxy, either the F658N or F657N narrow-band filter was used, selected according to the galaxy's systemic velocity to capture the Hα 6563 Å line. The observations were configured to maximise overlap with the five broad-band filters from the PHANGS-HST Treasury Survey (F275W, F336W, F438W, F555W, and F814W; Cycle 26, PID 15654; PI Lee), ensuring robust continuum subtraction and synergy with the stellar population data.

Prior to continuum subtraction, both the narrow-band (F658N or F657N) and the adjacent broad-band filters (F555W and F814W) were background-subtracted using synthetic filter images generated from the PHANGS-MUSE observations and corrected for Milky Way foreground extinction. The continuum-subtracted narrow-band images were then corrected for contamination by the [N II]λ6548 and [N II]λ6583 emission lines using PHANGS-MUSE spectroscopy.

The final HST Hα maps achieve an angular resolution of ~0.1″ (corresponding to ~2.5–10 pc across the sample) with a pixel scale of 0.04″ (~1–4 pc). This procedure yields high-fidelity emission-line maps for each galaxy, which form the basis of the following analysis (see Chandar et al. 2025 for further details).

2.4. PHANGS-HST association catalogues

In order to investigate the connection between ionised nebulae and their associated stellar populations, we make use of the multi-scale stellar association catalogues produced as part of the PHANGS–HST high-level data products (Larson et al. 2023). These catalogues provide a comprehensive census of stellar populations, encompassing both compact clusters and diffuse associations. This contrasts with the compact cluster catalogues, which primarily trace the densest peaks of star formation and omit much of the lower-density component (Maschmann et al. 2024).

The identification process begins with point-like sources detected in the HST images using DOLPHOT (Dolphin 2016), based on either NUV- or V-band photometry. A smoothed tracer image is then created by convolving the spatial distribution of sources to a set of predefined scales (typically 8, 16, 32, or

Table 1. Completeness statistics for number of nebula the MUSE and HST catalogues.

Galaxy	$N_{\rm MUSE,tot}$ # [1]	$N_{\rm MUSE}$ # [2]	N # [3]	f_N % [4]	$N_{C_{\rm simp}}$ # [5]	$N_{C_{\rm inter}}$ # [6]	$N_{C_{\rm comp}}$ # [7]	$N_{\rm HII}$ # [8]	$N_{\rm HII,ne}$ # [9]	$N_{\rm HII,assoc}$ # [10]
IC 5332	786	756	37	4.9	36	1	0	36	12	29
NGC 1087	1004	995	276	27.7	186	63	27	274	127	170
NGC 1300	1448	1437	229	15.9	155	59	15	216	84	109
NGC 1365	1409	888	193	21.7	105	38	50	141	74	86
NGC 1385	1023	1023	308	30.1	174	69	65	305	193	190
NGC 1433	1717	1018	142	13.9	99	27	16	114	34	67
NGC 1512	623	489	87	17.8	63	11	13	81	28	55
NGC 1566	2330	2049	470	22.9	288	110	72	439	242	338
NGC 1672	1559	1535	414	27.0	249	89	76	385	207	256
NGC 2835	1068	1007	188	18.7	135	46	7	176	120	128
NGC 3351	1247	1046	85	8.1	64	13	8	76	31	62
NGC 3627	1598	1122	280	25.0	187	54	39	262	157	192
NGC 4254	2940	2464	762	30.9	482	212	68	742	396	532
NGC 4303	3029	2650	702	26.5	438	180	84	674	385	465
NGC 4321	1806	1265	327	25.8	214	68	45	308	145	230
NGC 4535	1891	1523	204	13.4	162	35	7	193	77	114
NGC 5068	1781	1699	125	7.4	104	17	4	123	98	103
NGC 628	2773	2216	217	9.8	166	44	7	210	83	143
NGC 7496	758	728	131	18.0	79	33	19	127	51	80
Total	30 790	25 910	5177	20.0	3386	1169	622	4882	2544	3349

Notes. [1] The total number of nebulae within the MUSE catalogue for each galaxy (excluding flagged regions; see Groves et al. 2023). [2] The total number of MUSE nebulae catalogue within the HST coverage. [3] The total number of nebulae within the HST catalogue (excluding flagged regions; see Sect. 3.2). [4] Percentage of regions from the MUSE nebulae catalogue in the HST catalogue. [5, 6, 7] The total number of nebulae with a complexity scores (C) of $C \leq 1$ ($C_{\rm simp}$), $2 \leq C \leq 5$ ($C_{\rm inter}$), $C > 5$ ($C_{\rm comp}$) within the HST catalogue (see Sect. 3.4). [8] The total number of nebulae classified as H II regions within the HST catalogue. [9] The total number of nebulae classified as H II regions with reliable $n_{\rm e}$ estimates within the HST catalogue (see Sect. 5.2). [10] The total number of nebulae classified as H II regions within the HST catalogue and that have stellar properties from the NUV-selected multi-scale stellar associations at a scale of 32 pc (see Sect. 3.6).

64 pc). Local background subtraction is performed by removing a version of the tracer image smoothed to four times the original scale. The watershed algorithm (van der Walt et al. 2014) is then applied to the background-subtracted tracer image to delineate the boundaries of stellar associations, identified as localised overdensities at each scale. Photometry of the stars within each association provides fluxes across the five HST filters, which are then used to derive ages, masses, and extinctions by fitting theoretical single stellar population models (Bruzual & Charlot 2003) with CIGALE (Boquien et al. 2019), assuming a fully sampled initial mass function (Chabrier 2003). Caveats associated with these catalogues – particularly concerning the reliability of the lowest masses and youngest ages – are discussed in Section. 3.6.

3. PHANGS-MUSE/HST-Hα nebulae catalogue

The PHANGS-MUSE/HST-Hα nebulae catalogue is constructed using the PHANGS-MUSE nebulae catalogue as a prior (see Fig. 2). This "top-down" approach – applying the MUSE nebulae as masks before running source identification on the HST images – is preferred over a "bottom-up" method, where structures are first identified in the HST images and then matched to MUSE nebulae. The top-down method ensures direct consistency with the PHANGS-MUSE catalogue, facilitates the incorporation of MUSE spectroscopic information, and mitigates the risk of incompleteness introduced by the lower surface brightness sensitivity of the HST narrow-band imaging. While the HST observations provide higher spatial resolution (and therefore increased complexity), they are also intrinsically less sensitive to diffuse, low-surface-brightness emission than the MUSE data (Chandar et al. 2025). A similar top-down methodology was adopted by Barnes et al. (2022) to identify and analyse a small sample of H II regions in NGC 672.

3.1. Data homogenization

This process of identifying and cataloguing the sources within each galaxy was challenging due to the range in spatial scales and complexity of each nebula. This is a result of the factor of ~4 range of physical resolution achieved across the galaxy sample, the varying noise profiles within and among individual galaxies (see Chandar et al. 2025), as well as the inherent nature of the nebulae themselves.

To mitigate these effects, and to provide a consistent analysis across all galaxies in the sample, we homogenised the PHANGS-HST Hα images before performing our source identification (Sect. 3.2). This was a two-step process:

1. Resolution normalisation: All images were convolved to a fixed physical resolution of 10 pc, assuming a Gaussian point-spread function (PSF). This corresponds to the angular resolution of HST at a distance of 20 Mpc and is close to the lowest physical resolution in our sample (NGC 1365 at 19.6 Mpc; see Table B.1).
2. Noise normalisation: For each galaxy, a Gaussian noise map was generated and smoothed using the same Gaussian kernel as applied to the science data. The smoothed

noise maps were scaled such that, when added in quadrature to the observed images, the resulting maps achieved a uniform noise level with standard deviation $\sigma_{\rm final,10pc} = 6.25 \times 10^{-16}$ erg/s/cm^2/arcsec^2 (see Appendix I for additional details and caveats). This value was chosen as the maximum noise level measured across the 10 pc-smoothed images.

The procedure above produced maps with the same physical resolution and noise levels, which we will use for the following source identification.

3.2. Source identification

We begin by applying the PHANGS-MUSE nebula masks to the homogenised PHANGS-HST Hα images. Adopting a top-down approach, each of the 25 910 MUSE nebulae located within the overlapping coverage is analysed individually. A series of methods for source identification in the HST Hα images were tested; we ultimately adopted a threshold-based masking procedure, which offered a straightforward and reproducible means of isolating emission features across the full dynamic range and diverse morphologies in the sample.

This approach follows the two-threshold Boolean masking technique originally developed for molecular cloud identification in spectral line data cubes (Rosolowsky & Leroy 2006) and subsequently implemented for the PHANGS–ALMA survey (Leroy et al. 2021; Rosolowsky et al. 2021). Adapting this framework to our HST narrow-band imaging, we use a high threshold of $5\sigma_{\rm final,10pc}$ and a low threshold of $2\sigma_{\rm final,10pc}$ (see Sect. 3.1). For each masked MUSE nebula, binary masks are first generated at both thresholds. Structures smaller than three times the smoothed PSF area are removed from the low-threshold mask, since regions smaller than this are unlikely to yield reliable physical measurements, while the high-threshold mask is pruned of sources smaller than one PSF area to exclude spurious compact peaks. The cleaned high-threshold mask is then grown into the low-threshold mask, ensuring that compact, high-surface-brightness emission is retained while simultaneously recovering fainter diffuse substructure. This procedure also suppresses isolated noise fluctuations that would otherwise bias size and flux estimates. Finally, any internal holes are filled by including all pixels within the outermost contiguous boundary, so that each nebula mask corresponds to a single, continuous region.

Potential contaminants within the catalogue were assessed through a combination of parameter-based criteria and manual inspection. Firstly, flags were assigned to regions intersecting the edges of the HST coverage, following the convention established in the MUSE catalogue (Groves et al. 2023). An additional flag was used to identify regions in contact with neighbouring sources, which may form part of a larger complex. Secondly, a detailed manual inspection was conducted to identify residual contaminants. These typically manifest as small noise peaks, artefacts, or sources exhibiting luminosities significantly higher than expected relative to MUSE. A total of 576 regions were examined, selected based on either a physical size smaller than 10 pc, fewer than 20 pixels, or luminosities exceeding the MUSE measurements, specifically where $L_{\rm H\alpha}({\rm HST})/L_{\rm H\alpha}({\rm MUSE}) > 1$. Among these, we identified 30 bright foreground stars not effectively flagged in the MUSE catalogue, typically characterised by high-luminosity point sources, strong counterparts in the HST broadband images, and prominent negative artefacts in the continuum-subtracted Hα images. In addition, 54 cosmic rays or image artefacts were identified, appearing as compact, bright point sources, often located near the edges of the map. A single background galaxy was also flagged in NGC 1087. All identifications have been incorporated into an additional dedicated manual check flag within the catalogue.

The final catalogue comprises 5467 nebulae in the PHANGS-HST-Hα maps across the galaxy sample, corresponding to approximately one fifth of the total number of nebulae identified in the PHANGS-MUSE catalogue within the matched area (25 910). Incorporating the HST edge flags, MUSE edge flags, and manual contamination flags described above, we obtain a total of 5177 regions. This set constitutes the primary science sample used for all statistical analyses and figures in this work, unless otherwise stated.

3.3. Nebula properties, sizes, and luminosities

The physical properties of each nebula identified in the PHANGS-HST-Hα images are compiled into a unified catalogue. Each entry in the PHANGS-MUSE/HST-Hα nebula catalogue corresponds directly to a unique region in the PHANGS-MUSE nebula catalogue. The final combined catalogue thus contains the full set of nebular parameters from the MUSE-based catalogue described in Groves et al. (2023), including updated auroral-line fits and derived properties from Brazzini et al. (2024), as well as the additional parameters derived from the HST Hα data in this work (e.g. size and luminosity).

The physical size of each nebula is estimated using two complementary definitions. The first is the circularised radius, defined as $r_{\rm circ} = \sqrt{A/\pi}$, where A is the projected area enclosed by the source mask. This definition is consistent with that adopted for the MUSE catalogue. The second is the second-moment radius, $r_{\rm mom}$, computed as the geometric mean of the intensity-weighted second spatial moments of the emission within the source boundary (see Sect. 4.2 for a comparative analysis of $r_{\rm circ}$ and $r_{\rm mom}$).

The total Hα flux of each region is calculated by summing the flux within all pixels enclosed by the final source mask. This flux is compared to the corresponding MUSE-based flux measurements in Appendix D. To estimate extinction-corrected Hα fluxes and luminosities, we correct for the per-region dust-extinction in the PHANGS-MUSE catalogue. The corresponding Hα luminosity is computed as $L_{\rm H\alpha} = 4\pi D^2 F_{\rm H\alpha}$, where D is the distance to the galaxy and $F_{\rm H\alpha}$ is the extinction-corrected flux.

3.4. Complexity score

A limitation of our source identification method is its inability to separate multiple sources within a single PHANGS-MUSE catalogue mask (e.g. Figs. 1 and 2). This leads to source confusion in regions of high structural complexity, where overlapping nebular substructures are not individually resolved (see also Fig. C.1).

To provide a quantitative measure of this internal substructure, we perform a hierarchical segmentation analysis using the ASTRODENDRO software (Rosolowsky et al. 2008), applied to the flux distribution within the final HST catalogue mask of each region. The segmentation parameters were chosen to match those adopted in our initial source identification (see Sect. 3.3): the minimum number of pixels per structure is set to include one 10 pc resolution element (MIN_NPIX); the minimum flux threshold is set to MIN_VALUE = $2\sigma_{\rm final,10pc}$; and the minimum isocontour separation is MIN_DELTA = $5\sigma_{\rm final,10pc}$.

For each nebula, we define a complexity score (C) as the total number of dendrogram structures identified at all hierarchical levels. This metric is intended primarily as a relative proxy for structural richness rather than an absolute measurement. While

the exact value of C varies with the adopted thresholds, tests varying the parameters by factors of two confirm that the relative ranking of regions is preserved: nebulae classified as complex remain distinct from those with simple morphologies. In this sense, C provides a practical first-order indicator of relative complexity. The resulting scores range from 0 to ∼100 and are grouped into three broad categories:

- $C_{\rm simp}$: A score of $C \leq 1$ (3386 regions) identifies nebulae with relatively simple morphology. These typically consist of a single weak and diffuse structure ($C = 0$), or a single compact or brighter diffuse component ($C = 1$).
- $C_{\rm inter}$: Regions with $2 \leq C \leq 5$ (1169 regions) exhibit modest substructure, such as multiple compact emission peaks or a combination of diffuse and clumpy features.
- $C_{\rm comp}$: A score of $C > 5$ (622 regions) corresponds to morphologically complex nebulae, containing numerous substructures.

The classification thresholds were set empirically to best reflect the observed morphologies. Representative examples are shown for NGC 1566 in Fig. 2 (lower left), alongside the corresponding HST Hα emission (upper right), with further examples in Fig. C.1. These illustrate that the adopted categories capture the broad contrast between simple, intermediate, and complex nebulae. To preserve flexibility, the individual C values are reported in the catalogue, so that alternative thresholds can be adopted if required by future analyses. Table 1 lists the number of regions in each category per galaxy.

3.5. H II region properties

We find that 4882 nebulae, corresponding to approximately 94% of the total 5177 sample, are classified as H II regions using the emission-line diagnostics outlined in Groves et al. (2023). For this subset, we derive additional physical properties, including electron densities and ionising photon production rates.

Electron densities, $n_{\rm e}$, are determined using the PyNeb package (Luridiana et al. 2015)[2], which solves the equilibrium level populations for user-defined ionic species. For each H II region, $n_{\rm e}$ is computed from the flux ratio $R_{[S\,II]} = F_{[S\,II]\lambda6716}/F_{[S\,II]\lambda6731}$, combined with an assumed electron temperature, $T_{\rm e}$. We adopt measured values of $T_{\rm e}$ from Brazzini et al. (2024), derived from the Nitrogen auroral line ratio, where available. In total, 779 H II regions (14% of the sample) have such measurements. For the remaining majority, we assume a representative value of $T_{\rm e} = 8000$ K, which corresponds to the mean of the measured values (standard deviation is 1800 K)[3].

The $R_{[S\,II]}$ diagnostic saturates in the low- and high-density regimes, approaching values of ∼1.45 for $n_{\rm e} \lesssim$ a few 10 cm^{-3}, and ∼0.4 for $n_{\rm e} \gtrsim$ a few 10^3 cm^{-3}. Within this range, $R_{[S\,II]}$ provides a robust estimate of the [S II]-weighted mean electron density of the ionised gas. Following Barnes et al. (2021), we exclude regions where $R_{[S\,II]}$ lies within 3σ of the low-density limit, to avoid unreliable estimates[4]. After applying these criteria, we obtain reliable $n_{\rm e}$ estimates for 2544 H II regions – approximately half of the sample. This is comparable to the number of regions with $n_{\rm e}$ measurements in the full MUSE sample (Barnes et al. 2021), indicating that the vast majority of denser sources are recovered here[5].

We also estimate the ionising photon production rate, Q, for each region under the assumption of Case B recombination and optically-thick conditions. For an electron temperature of $T_{\rm e} = 8000$ K and $n_{\rm e} < 10^6$ cm^{-3}, $Q \approx L_{\rm H\alpha}/(0.45\,h\nu_{\rm H\alpha})$, where $L_{\rm H\alpha}$ is the extinction-corrected Hα luminosity (derived from the HST Hα flux), h is Planck's constant, and $\nu_{\rm H\alpha}$ is the frequency of the Hα transition. The factor 0.45 represents the fraction of total hydrogen recombinations that produce Hα emission at this temperature (see Storey & Hummer 1995; Osterbrock & Ferland 2006; Byler et al. 2017, also Tab. 14.2 in Draine 2011).

3.6. Stellar properties

To connect the physical properties of the ionised gas within H II regions (see Sect. 3.3) to their underlying stellar populations, we link each region to the PHANGS-HST stellar associations catalogue (see Sect. 2.4). An example is shown in of Fig. 2 (lower left), with additional examples illustrated in Figs. C.1. This procedure follows the method introduced by Scheuermann et al. (2023), who matched stellar associations from HST to the PHANGS-MUSE nebulae catalogue.

We construct a matched catalogue by identifying cases where the HST nebula mask of a given H II region spatially overlaps with one or more stellar associations. A match is accepted if any part of the association boundary lies within the boundary of the PHANGS-MUSE/HST-Hα nebula mask. If multiple associations are found within a single nebula mask[6], we flag the region accordingly and adopt the properties of the *youngest* stellar association, under the assumption that it is most likely to be responsible for the observed ionisation.

The matching includes associations identified at all spatial scales (8, 16, 32, and 64 pc) and in both the NUV- and V-band multi-scale association catalogues. However, in the analysis that follows, we focus on the 32 pc-scale associations derived from the NUV images. As shown by Scheuermann et al. (2023), the NUV selection better traces young, massive stars, while the 32 pc scale provides a good match to the resolution of the MUSE data. A total of 3349 H II regions (64% of the sample) are matched with at least one NUV-selected 32 pc-scale stellar association. A per-galaxy breakdown is provided in Table 1.

Table H.3 summarises the 10th, 50th (median), and 90th percentiles of the age and stellar mass (log scale) distributions of the matched associations across the sample. The stellar mass distribution is dominated by associations in the range $\log(M_*/{\rm M}_\odot) = 3.5$–$4.5$, although several galaxies contain more massive associations (with 90th percentile $\log(M_*/{\rm M}_\odot) > 5$). These higher-mass associations are typically found in galaxies with elevated star formation rates. For example, NGC 1365 – the most actively star-forming galaxy in our sample – hosts the most massive associations in terms of median stellar mass.

We find that the median ages vary modestly between galaxies, reflecting differences in recent star formation history and evolutionary stage, but the overall distribution is strongly peaked

[2] PyNeb version '1.1.24', which includes atomic information for S II taken from Tayal & Zatsarinny (2010) and Rynkun et al. (2019).

[3] The electron temperature is computed from the auroral-to-nebular line ratio ([N II]λ6584 + [N II]λ6548)/[N II]λ5755, using PyNeb with an assumed density of 100 cm^{-3}. The derived $T_{\rm e}$ values are insensitive to this assumption at the typical densities of our sample (<1000 cm^{-3}; see Méndez-Delgado et al. 2023).

[4] We correct the [S II] flux uncertainties from the Groves et al. (2023) catalogue following Barnes et al. (2021), with a temperature-dependent lower limit estimated using PyNeb. We find a slightly larger correction factor of 1.53, compared to the original value of 1.38.

[5] Note that a slightly different version of the PHANGS-MUSE catalogue is used in this work.

[6] For example, in the sample of 32 pc-scale NUV-selected associations, 25% of matched H II regions are associated with more than one stellar association.

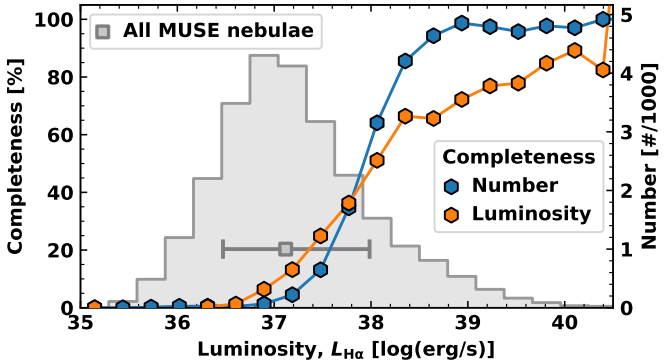

Fig. 3. Catalogue completeness. Shown is the number (also see Table 1) and luminosity completeness for the HST catalogue with respect to the MUSE catalogue as a function of luminosity, log($L_{H\alpha}$). Also shown as a grey histogram (second y-axis) is the total number of regions within the MUSE catalogue within each luminosity bin, where the grey point with error bars shows the median and standard deviation of the distribution.

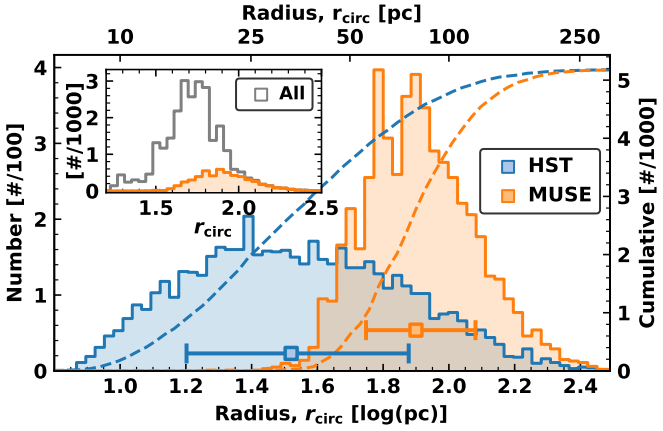

Fig. 4. Distribution of source sizes for all galaxies in the PHANGS-MUSE and PHANGS-MUSE/HST-Hα Nebula Catalogue. The histogram distributions of source radii for galaxies identified in both the HST and MUSE observations are shown in blue and orange, respectively. The points with error bars denote the median and standard deviation of the distributions. It is important to note that only sources detected by both HST and MUSE are displayed in the main panel, excluding the full MUSE sample identified by Groves et al. (2023). The distributions extend down to radii of approximately 5 pc, corresponding to the half-width at half-maximum (HWHM) of the assumed Gaussian point spread function (PSF) used to homogenise the observations (see Sect. 3.1). The inset panel presents the distribution of source radii for the full MUSE catalogue (restricted to the HST field of view), alongside those detected in the HST catalogue.

toward young associations, with a global median age of 3 Myr (see Fig. 12 for the full range of ages). This supports the expected interpretation that most H II regions are powered by the youngest stellar associations in each system.

Before proceeding, we note three important caveats. Firstly, the age distribution of associations exhibits a pronounced peak at 1 Myr (Fig. 12), which arises from an artefact of the SED-fitting methodology used in the PHANGS-HST catalogue (Larson et al. 2023). This bias, inherent to models excluding nebular emission (Bruzual & Charlot 2003), leads to an over-representation of 1 Myr ages, as discussed by Thilker et al. (2025). Consequently, associations assigned an age of 1 Myr should be interpreted as spanning 1–3 Myr. Future catalogue versions will incorporate improved models that include nebular emission (Thilker et al. 2025), resolving this degeneracy (see also Whitmore et al. 2025; Henny et al. 2025). Secondly, the assignment of a single age per H II region or complex does not capture the intrinsic age spread within these regions. Sequential star formation, often driven by feedback mechanisms (e.g. Elmegreen & Lada 1977; Walborn & Parker 1992; Walborn & Blades 1997; Whitmore et al. 2010, 2025), leads to a range of stellar ages, typically spanning 1–10 Myr. This age spread should be considered when interpreting analyses that assume coeval stellar populations. Thirdly, the stellar masses reported for associations with $\log(M_*/M_\odot) \lesssim 4$ should be regarded with some caution. At these low masses, stochastic sampling of the stellar initial mass function can introduce significant scatter in the derived properties, since the assumption of a fully populated Chabrier (2003) IMF is less appropriate. While such associations are retained in the catalogue for completeness, their mass estimates carry high uncertainties.

4. Nebulae catalogue properties

In this section, we provide an overview of key properties derived from the PHANGS-MUSE/HST-Hα nebulae catalogue.

4.1. Structure and completeness

As illustrated in Fig. 2 (see also Fig. C.1), the order-of-magnitude improvement in angular resolution provided by HST relative to MUSE enables a significantly more detailed view of the internal structure of the nebulae. In this example, taken from NGC 1566 (Chandar et al. 2025), the HST data reveal compact emission peaks and substructures that are unresolved in the MUSE observations. Moreover, the HST emission appears more spatially confined, predominantly tracing the higher surface brightness components, while the MUSE data capture more extended, diffuse emission due to their higher surface brightness sensitivity.

In Fig. 3, we present the completeness of the HST catalogue as a function of MUSE Hα luminosity, measured both in terms of the number of recovered regions and their cumulative luminosity. Completeness is computed per luminosity bin by comparing the subset of MUSE nebulae that are matched to HST detections with the total number or luminosity of MUSE nebulae in that bin. At the peak of the MUSE luminosity function ($\log L_{H\alpha} \sim 37$), the completeness in number is approximately 5%, and in luminosity, approximately 10%. The 50% completeness thresholds in both number and luminosity are reached at $\log L_{H\alpha} \sim 38$. For brighter regions ($\log L_{H\alpha} > 38.5$), the completeness rises to 90% in number and 75% in luminosity.

These results confirm that the PHANGS-MUSE/HST-Hα catalogue is significantly more complete for higher-luminosity nebulae in the MUSE sample, with reduced sensitivity to diffuse, low-luminosity regions due to the limitations of our HST narrow-band imaging.

4.2. Size

4.2.1. Comparison of HST and MUSE sizes

In Fig. 4, we present the distribution of circularised radii measured from both the PHANGS-MUSE and PHANGS-HST-Hα observations across the full galaxy sample. We find that the radii of sources in the MUSE catalogue are clustered around

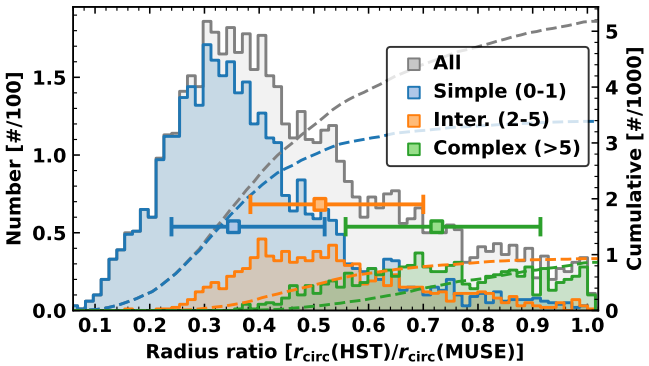

Fig. 5. Distribution of source sizes ratios for all galaxies in the Nebula Catalogues relative to MUSE. The ratio of the size of each region identified in both the HST or MUSE observations for all nebulae in the sample is shown in grey. The ratio of the sizes split between complexity scores of 0–1, 2–5, and >5, denoting simple and intermediate and complex regions, respectively are shown as coloured histograms (see Sect. 4.1).

70 pc, consistent with the average linear resolution limit of the MUSE observations for this galaxy sample (see also Barnes et al. 2021; Santoro et al. 2022; Groves et al. 2023), and as listed in Table B.1. By contrast, the HST-based radius distribution is broader, with a peak around 20 pc and values extending down to the fixed resolution limit of ∼10 pc.

The ratio of HST to MUSE circularised radii, r_{circ}(HST)/r_{circ}(MUSE), is shown as a grey histogram in Fig. 5. The distribution peaks at a ratio of approximately 0.3 and declines smoothly between ∼0.1 and 1.0. By construction, the HST-defined nebulae are constrained to lie within the corresponding MUSE masks, and therefore this ratio cannot exceed unity.

Also shown in Fig. 5 (coloured histograms) is the distribution of size ratios subdivided by complexity score class (C_{simp}, C_{inter}, C_{comp}; see Sect. 3.4). Regions with high size ratios ($r_{HST}/r_{MUSE} > 0.6$) are predominantly found among the complex class (C_{comp}), whereas regions with low size ratios (<0.4) are dominated by simple nebulae (C_{simp}). This indicates that large HST–MUSE size ratios typically arise from spatially blended or confused regions in the MUSE data – corresponding to complex, extended emission – while smaller ratios reflect more compact, isolated nebulae well resolved by HST. Given the correlation between size and Hα luminosity (see Fig. 9), this also implies that more luminous nebulae tend to be more complex.

To assess how these ratios vary across different galactic environments, we show in Fig. 6 the distribution of HST/MUSE size ratios as a function of environment classification, following the definitions in Querejeta et al. (2021). Regions located in galaxy centres show the highest fraction (approximately 25%) of near-unity size ratios, consistent with expectations of crowding and structural complexity, as well as higher and more complex background, diffuse emission, in the central regions (see also Fig. 1)[7]. In contrast, the bar, arm, inter-arm, and disc environments exhibit lower fractions of high-ratio regions. Each of these environments contains at least 50% of its regions with HST/MUSE size ratios below 0.4.

A Kruskal–Wallis test (Kruskal & Wallis 1952) confirms significant differences across the five environments ($H = 432.3$, $p < 0.001$). Pairwise Kolmogorov–Smirnov tests show that the centre differs significantly from all other regions (KS = 0.54–0.64; $p < 0.001$). While the non-central environments are broadly similar, significant differences exist between most pairs (KS ∼0.1; $p < 0.05$), except for the inter-arm and disc, which do not differ significantly (KS = 0.048; $p = 0.27$).

4.2.2. Comparison of HST sizes to other surveys

We also compare the size distribution derived from the PHANGS-MUSE/HST-Hα catalogue with that obtained in higher spatial resolution extragalactic and Galactic studies. As shown in Fig. 7, the radius distribution of our sample closely matches that of NGC 300 observed with MUSE (at a distance of around 2 Mpc, the achieved resolution of ∼1″ matches our homogenised spatial resolution of 10 pc; McLeod et al. 2021). This agreement reflects the similarly high spatial resolution achieved in both datasets, enabling detection of compact H II regions down to scales of a few parsecs. We note that this comparison is most appropriate for the subset of simple regions in our catalogue (C_{simp}), which are expected to best represent isolated, well-resolved nebulae in external galaxies.

In contrast, the distribution of Galactic H II region sizes from Anderson et al. (2014) peaks at smaller values. This is attributable to the higher linear resolution (at sub-pc for the closest regions) achievable within the Milky Way, as well as to differences in selection methodology (i.e. using different emission – dust and PAH emission – to identify their regions). In particular, their catalogue is constructed from 22 µm emission and likely includes a large number of very young, embedded H II regions that are optically obscured and intrinsically smaller in physical size.

The PHANGS-MUSE/HST-Hα sample includes a broader distribution of sizes, extending to significantly larger radii due to the presence of more complex and blended regions, particularly in crowded environments. Nevertheless, the overlap in the size distributions with both Galactic and extragalactic studies supports the reliability of our catalogue in capturing a representative range of nebular sizes, particularly among the more luminous and spatially extended H II region population.

4.2.3. Comparison of HST sizes (r_{circ} vs r_{mom} vs $r_{mom,deconv}$)

A potential limitation of using the circularised radius, r_{circ}, as a size metric is its sensitivity to both the intrinsic emission morphology of the region and the local noise properties of the observations. In particular, extended low-surface-brightness wings or fragmented structures can artificially increase the enclosed area, leading to overestimated sizes. To mitigate this, we also consider an alternative size definition based on the intensity-weighted second spatial moment of the Hα emission, denoted r_{mom}. This moment-based size is further deconvolved with the 10 pc FWHM point-spread function, assuming a Gaussian profile, following the relation $r_{mom,deconv} = \sqrt{r_{mom}^2 - \sigma_{PSF}^2}$ where $\sigma_{PSF} = FWHM/\sqrt{8 \ln 2}$ corresponds to the standard deviation of the (assumed to be Gaussian) point-spread function.

[7] The segmentation used to construct the PHANGS–MUSE catalogue is known to struggle in very crowded circumnuclear environments, such as starburst rings (e.g. NGC 1300, NGC 1512, NGC 1672, NGC 3351, NGC 4303, NGC 4321) and in galaxies hosting low-luminosity AGN (e.g. NGC 1365, NGC 1512, NGC 1566, NGC 1672; see Santoro et al. 2022; Groves et al. 2023). In these environments, deblending individual H II regions is not possible at the MUSE resolution, which then contributes to the larger and more complex nebulae we recover in the central regions. These regions are nonetheless included in the catalogue presented here, but their derived sizes should be interpreted with caution.

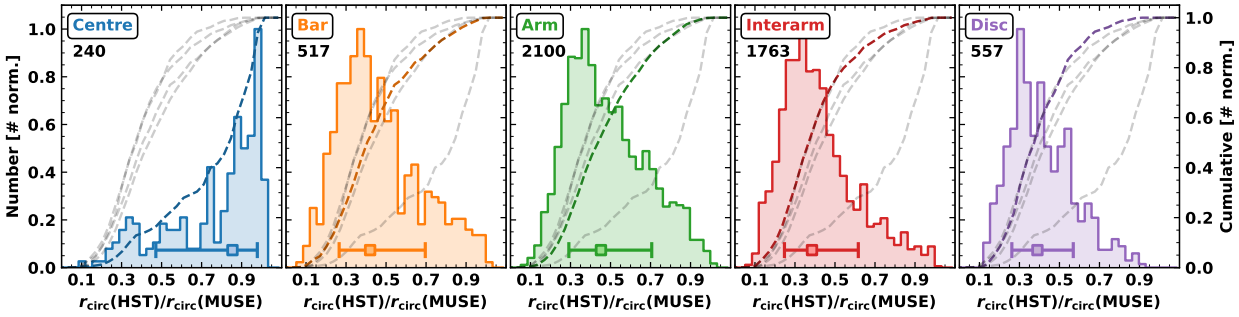

Fig. 6. Distribution of source size ratios (HST/MUSE) in the nebula catalogue within each environment (Querejeta et al. 2021). Shown is the ratio of the size of each region identified in both the HST or MUSE observations (see Fig. 4 for full distribution, and see Fig. F.1 for distribution of r_{circ} for each environment). We show the histogram and cumulative distributions as solid filled and dashed lines, respectively (see upper left number of regions in each histogram). For comparison, all distributions are normalised to unity and overlaid on each panel as light dashed grey lines are the cumulative distributions from the other panels.

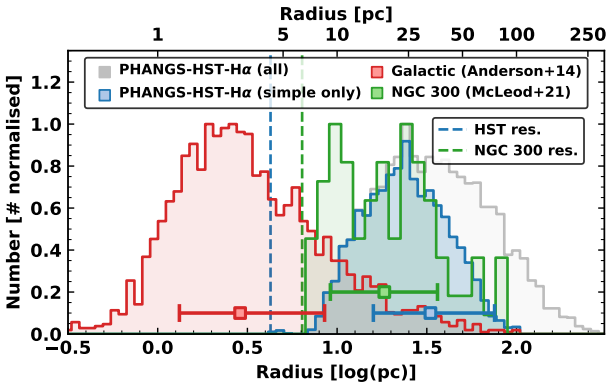

Fig. 7. Comparison of radius distributions across samples. Normalised histogram of nebular (r_{circ}) radii (log scale) for the PHANGS-HST-Hα catalogue (C_{simp} regions only are shown in filled blue, whilst the histogram for all regions is shown in grey), compared with Galactic H II region data from Anderson et al. (2014) and observations of NGC 300 from McLeod et al. (2021). Vertical dashed lines indicate the approximate resolution limits of the HST (blue) and NGC 300 (green) datasets.

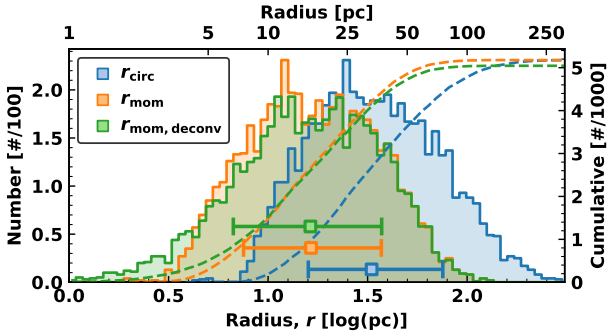

Fig. 8. Comparison of the sizes obtained by the circular and the moment methods (see Sect. 4.2). We show the histogram and the cumulative distribution for both the circular (r_{circ}; blue), the moment definition of the radius (r_{mom}; orange) and the deconvolved moment ($r_{mom,deconv}$; green).

In Fig. 8, we compare the distributions of r_{mom}, $r_{mom,deconv}$ and r_{circ} across the PHANGS-MUSE/HST-Hα catalogue. The r_{mom} and $r_{mom,deconv}$ distributions are systematically shifted toward smaller radii, with a peak near 10 pc, while r_{circ} peaks around 20–25 pc. The distribution of the r_{mom}/r_{circ} ratio peaks just below a value of 0.5, similar to the ratio between the standard deviation of a Gaussian profile and its half-width at tenth maximum (HWTM), for which σ/HWTM $\approx$ 0.47.

This then reflects the different physical interpretations of each metric: r_{mom} (and $r_{mom,deconv}$) is most analogous to the standard deviation of the surface brightness distribution, providing a compactness-weighted size, whereas r_{circ} reflects the total projected area above a threshold, more sensitive to irregular shapes and diffuse substructure. The difference between these two estimators is therefore a useful diagnostic of nebular morphology and may serve as a proxy for structural concentration.

5. Analysis

5.1. Recovering sizes for unresolved regions

Although a substantial number of H II regions are recovered in our HST-based catalogue (5177), a large fraction of those detected by MUSE remain undetected. Specifically, ~80% of the MUSE nebulae within the matched field of view are not identified in the HST data. Hence, to estimate the size distribution for this large population, we adopt the methodology introduced by Pathak et al. (2025)[8], which involves calibrating a luminosity–size relation using MUSE-derived Hα luminosities and HST-based size measurements.

Figure 9 shows the resulting luminosity–size distributions for various combinations of luminosity and size measurements from MUSE and HST. These distributions span approximately two orders of magnitude in radius and four orders of magnitude in luminosity. We see tight correlation using resolved size estimates from the HST catalogue comparing to either the luminosity measured from the HST or MUSE. We fit a linear function in log–log space to both the median-binned and all the points within a 1–99 percentile range (see Figure 9). The fits are given as the following:

Point fits:

$$\log(r_{circ}) = 0.479\log(L_{H\alpha}) - 16.820, \quad (1)$$
$$\log(r_{mom}) = 0.467\log(L_{H\alpha}) - 16.678, \quad (2)$$
$$\log(r_{mom,deconv}) = 0.523\log(L_{H\alpha}) - 18.859. \quad (3)$$

Bin fits:

$$\log(r_{circ}) = 0.451\log(L_{H\alpha}) - 15.742, \quad (4)$$
$$\log(r_{mom}) = 0.428\log(L_{H\alpha}) - 15.194, \quad (5)$$

[8] The results presented here differ slightly from those of Pathak et al. (2025), who used an earlier internal release of the HST catalogue at native resolution and noise levels.

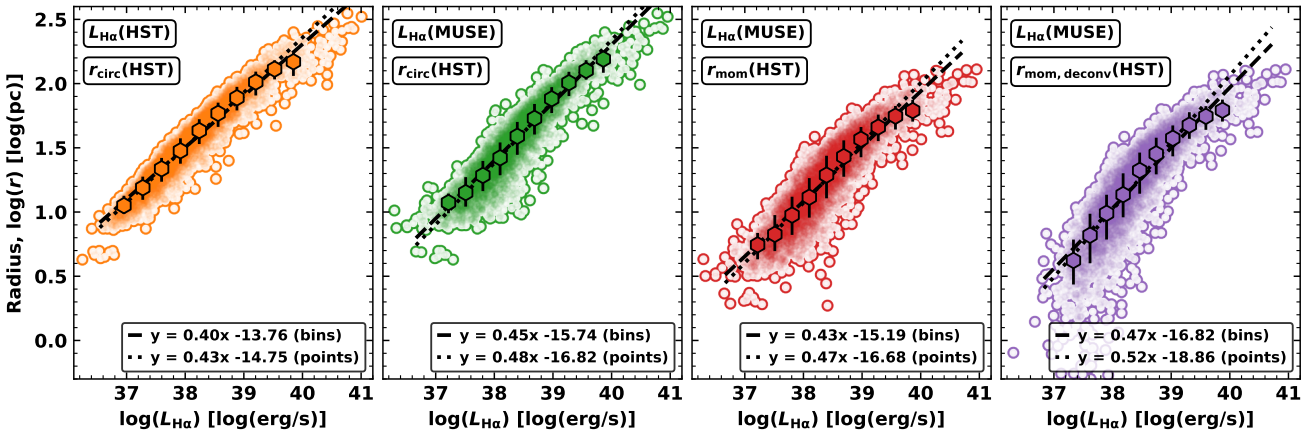

Fig. 9. Luminosity-size (log–log) distribution for all galaxies. The distributions of circular radius (r_{circ}) as a function of luminosity, $L_{H\alpha}$(HST), measured in the HST images (first panel). The circular (r_{circ}; second panel), moment (r_{mom}; third panel), deconvolved ($r_{mom,deconv}$; forth panel) radius from the HST catalogue as a function the luminosity, $L_{H\alpha}$(MUSE), from the MUSE catalogue. Overlaid are equally spaced binned points (median values of bins shown), with error bars indicating the standard deviation of the points within each bin. Also overlaid are the results of the fitting for the bins and points between the 1 and 99 percentile ranges in both $L_{H\alpha}$ and r (see legend and text for more details).

$$\log(r_{mom,deconv}) = 0.470\log(L_{H\alpha}) - 16.824. \quad (6)$$

We use these relations to scale the MUSE-derived Hα luminosities and recover corresponding radius estimates, which we denote $r_{lum,circ}$, $r_{lum,mom}$, or $r_{lum,mom,deconv}$.

This approach enables us to estimate sizes for the full sample of MUSE-detected nebulae, circumventing the completeness limits of the HST catalogue. Notably, the recovered distributions extend to significantly smaller physical scales, reaching down to ~1 pc in the case of $r_{lum,mom}$. This reflects the inclusion of lower-luminosity regions from the MUSE catalogue, which, under the assumed scaling relation, correspond to compact nebulae that would not be detected in the HST imaging.

We note that this method implicitly assumes a universal luminosity–size relation across all H II regions. While this is a strong assumption, it is physically motivated by the expected connection between stellar mass, ionising photon output, and nebular luminosity (e.g. Brown & Gnedin 2021). We demonstrate this in Section 5.3 (Fig. 13), where we show that Hα luminosity correlates strongly with the stellar masses of associated populations, supporting the use of this scaling relation for statistical recovery of sizes. However, if the regions undetected in the *HST* imaging are preferentially diffuse and spatially extended, then their sizes would be systematically underestimated. In this case, the use of a luminosity–size relation calibrated on higher surface brightness regions would map their MUSE-derived luminosities onto radii that are too small, primarily biasing the low-luminosity tail of the recovered size distribution and potentially distorting interpretations of the population's structural properties.

5.2. Systematic comparison to Strömgren sphere models

Here, we assess whether the observed sizes of H II regions are consistent with predictions from idealised Strömgren sphere models (Strömgren 1939). The expected radius of a Strömgren sphere is given by

$$r_{str} = \left(\frac{3Q}{4\pi\alpha_B(T_e)n_e^2}\right)^{1/3}, \quad (7)$$

where Q is the ionising photon flux, n_e is the hydrogen number density, and $\alpha_B(T_e)$ is the temperature-dependent case B recombination coefficient (in units of cm^3,s^{-1}). For $\alpha_B(T_e)$, we adopt the fitting formula from Hui & Gnedin (1997), based on Ferland et al. (1992):

$$\alpha_B(T_e) = 2.753\times10^{-14}\left(\frac{T_e}{315\,614}\right)^{-1.5}\left[1+\left(\frac{115\,188}{T_e}\right)^{0.4}\right]^{-2.2}, \quad (8)$$

where T_e is the electron temperature in Kelvin. For regions lacking direct temperature estimates from auroral lines (e.g. [N II]λ5755), we adopt a representative value of 8000 K (see Sect. 3.3).

Figure 10 compares the measured sizes of H II regions to the theoretical Strömgren radii computed from Eq. (7). We find that r_{str} is systematically smaller than all observed size estimates, with typical offsets ranging from factors of a few (compared to $r_{mom,deconv}$) up to an order of magnitude (relative to r_{circ}(MUSE)).

A natural interpretation of this discrepancy is that the ionised gas traced by [S II] emission occupies only a small fraction of the total nebular volume. Because the Strömgren radius scales as $r_{str} \propto n_e^{-2/3}$, electron densities inferred from [S II] are biased high in the presence of clumping or edge-brightened shells, which enhance the [S II] emissivity and thereby reduce the inferred r_{str}. This behaviour is expected from theoretical models and seen in resolved observations, where D-type ionisation fronts sweep up dense shells around expanding H II regions, and is consistent with the edge-brightened morphologies seen in our sample (e.g. see Weilbacher et al. 2015; McLeod et al. 2019; Kreckel et al. 2024 for resolved observation examples).

To quantify this effect, we estimate effective volume filling factors by comparing the predicted Strömgren radii to observed sizes (as introduced by Osterbrock & Flather 1959). The filling factor can be written as,

$$\epsilon = \frac{3Q}{4\pi\,\alpha_B(T_e)\,n_e^2\,r^3} = \frac{r_{str}^3}{r^3}, \quad (9)$$

where Q is the ionising photon rate, n_e the [S II]-derived electron density, and r the observed radius. This expression is equivalent to the formulation used in ionisation-parameter studies of

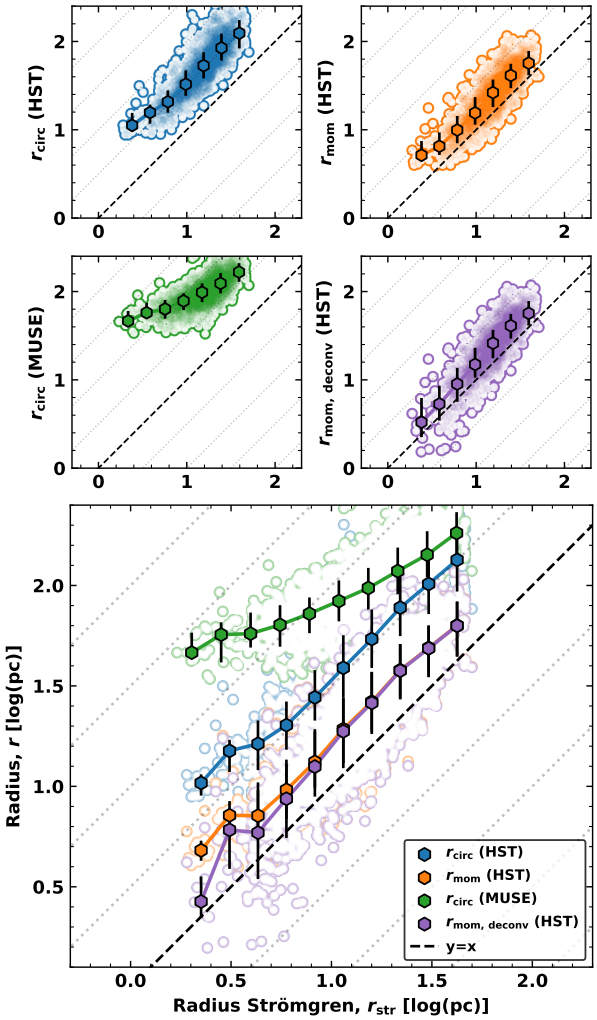

Fig. 10. Comparison of observed nebula sizes with theoretical Strömgren radii (Sect. 5.2). The top four panels (2 × 2) show, individually, r versus the Strömgren radius r_{str} for r_{circ} (HST), r_{mom} (HST), r_{circ} (MUSE), and $r_{mom,\,deconv}$ (HST), respectively. The bottom panel overlays all four measurements. In every panel, points are binned at equal intervals in r_{str}; symbols mark bin medians and error bars indicate the standard deviation of values within each bin. The $y = x$ relation is shown as a dashed black line (with faint dotted offset guides in the overlay).

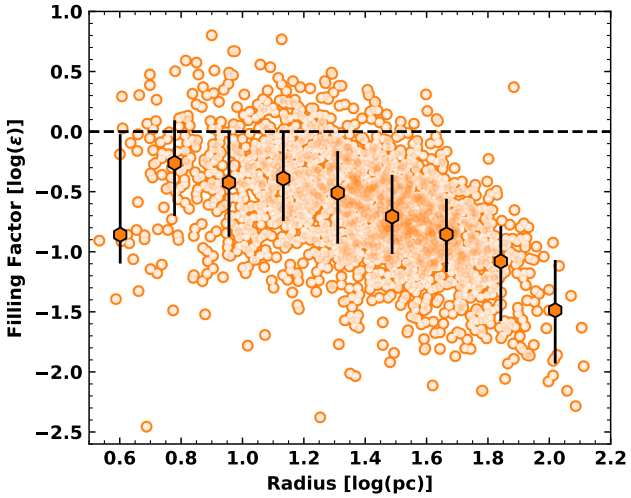

Fig. 11. Filling factors as a function of nebular size. The filling factor is computed from the Strömgren balance (Eq. (9)). Black hexagons with error bars show the median and ±1σ scatter in size bins. The dashed line marks $\epsilon = 1$, expected for a uniform-density Strömgren sphere. The systematically low values highlight the clumpy nature of the ionised gas, with [SII] tracing dense structures embedded within more extended nebulae.

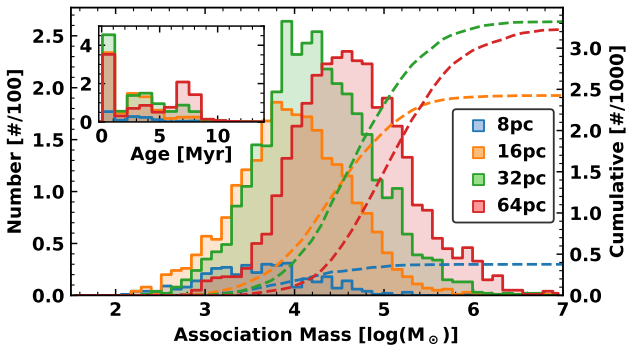

Fig. 12. Distribution of NUV-selected multi-scale stellar associations connected with the HST Nebula Catalogue (see Sect. 3.6). We show the histogram and the cumulative distribution for the stellar association masses (*main panel*) and ages (*inset panel*) as solid filled and dashed lines, respectively. Distributions are shown for stellar associations identified at scales of 8, 16, 32, and 64 pc (see Larson et al. 2023), including H II regions with both single and multiple associations. The 8 pc scale is not available for galaxies with distances larger than 18 Mpc (see Table B.1). Here, the 'scale' refers to the Gaussian-smoothing lengths used in the multi-scale watershed segmentation of Larson et al. (2023), and should not be confused with the physical radii of the H II regions measured in this work.

H II regions (e.g. Diaz et al. 1991). In Fig. 11, we show ϵ as a function of the moment-based radius (r_{mom}), which provides an upper-limit estimate of the filling factor. We find that compact regions on ∼10 pc scales approach $\epsilon \sim 1$ (completely filled), while progressively larger regions exhibit systematically lower values. Across the full sample we obtain a median $\epsilon = 0.22$ (mean 0.40), with a 10th–90th percentile range of 0.06–0.78. These values are consistent with independent determinations for nearby H II regions: Kennicutt (1984) reported typical filling factors of 0.01–0.1, while Cedrés et al. (2013) found values in the range 10^{-6}–10^{-1} with a similar decreasing trend of lower filling factors for larger regions. This reinforces the conclusion that [SII] preferentially traces dense, low-filling-factor structures embedded within larger ionised volumes.

5.3. Comparison to stellar properties

As shown in Fig. 12, the stellar mass and age distributions of the PHANGS–HST association catalogue (see Sects. 2.4 and 3.6) vary systematically with the adopted association scale. Note that here the 'scale' refers to the Gaussian-smoothing lengths used in the multi-scale watershed segmentation of (Larson et al. 2023), and should not be confused with the physical radii of the H II regions measured in this work. The stellar mass distributions are skewed toward lower-mass systems across all identification scales, with the median association mass decreasing from the 64 pc to the 8 pc smoothing scales. At the same time, the age distributions exhibit a secondary peak around 7 Myr at the largest (64 pc) scale, reflecting the fact that larger apertures encompass composite associations that blend multiple stellar populations of different ages and masses. By contrast, the smaller apertures preferentially isolate individual, younger, and lower-mass associations. This behaviour is consistent with the hierarchical nature

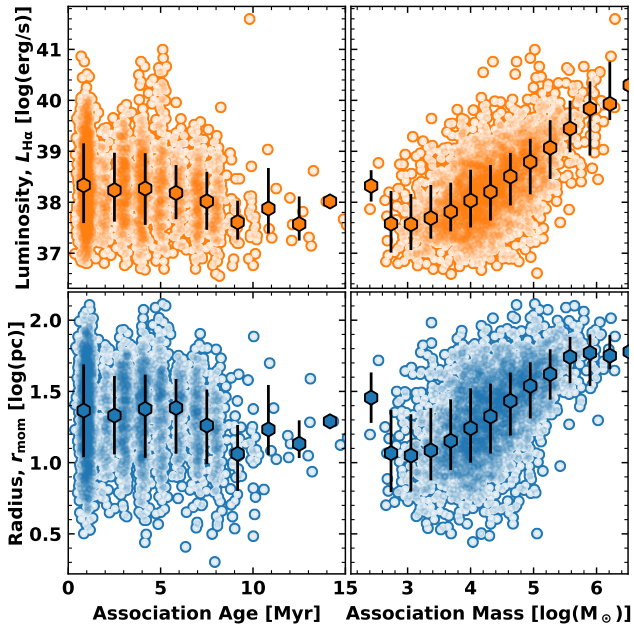

Fig. 13. Size and luminosity of the H II regions as a function of the stellar association age (left panels) and mass (right panels). The top row shows the attenuation-corrected Hα luminosity, while the bottom row shows the circularised radius. We show only the NUV-selected multi-scale stellar associations at a scale of 32 pc, which is comparable to Scheuermann et al. (2023). Overlaid are equally spaced binned points (median values per bin), with error bars indicating the 16th to 84th percentile range of the data within each bin.

of star formation, in which stellar structures are organised over a range of spatial scales, from sub-cluster groupings to larger associations and complexes (e.g. Grasha et al. 2017; Larson et al. 2023).

In Fig. 13, we explore the relationship between the Hα-defined H II region luminosity and size, and the mass of the associated stellar population (here using the 32 pc-scale, NUV-selected associations). A clear positive correlation is observed: more massive associations tend to power larger and more luminous ionised regions. This is consistent with theoretical expectations, where more massive clusters generate stronger ionising radiation fields, resulting in larger ionised volumes (e.g. Lopez et al. 2014), as predicted by classical Strömgren sphere models (Strömgren 1939).

In contrast, the left-hand panel of Fig. 13 shows little correlation between region size and association age. This suggests that, within our sample, the primary driver of nebular size is the mass of the powering stellar association, rather than its age. This interpretation is consistent with the rapid decline in UV luminosity beyond a few Myr (e.g. Leitherer et al. 1999) and with the relatively narrow age spread of the associated clusters.

5.4. Does DIG systematically bias line ratios in unresolved H II regions?

We assess whether diffuse ionised gas (DIG) significantly biases the nebular line ratios measured in unresolved H II regions in MUSE by examining correlations between emission-line diagnostics and spatial resolution, as traced by the radius ratio between HST and MUSE detections. Figure 14 presents the variation of several commonly used diagnostic ratios – [OIII]/Hβ, [NII]/Hα, [SII]/Hα, [OI]/Hα – along with Hα equivalent width, as a function of the HST-to-MUSE radius ratio (r_{HST}/r_{MUSE}).

To ensure that our analysis is not biased by shock-dominated sources, we have removed all supernova remnants (SNRs) and SNR candidates identified in the MUSE nebular catalogue by Li et al. (2024). In total, 556 (10% of our sample) such regions are excluded from this analysis, as SNRs typically exhibit elevated low-ionisation line ratios that would skew the trends under investigation.

In general, the emission-line ratios exhibit only weak or negligible dependence on the radius ratio (see Fig. 14). The exception is the Hα equivalent width, which increases steadily with radius ratio, likely reflecting the contribution of more extended, actively star-forming complexes in regions that are better resolved in the MUSE observations. Among the diagnostic line ratios, a mild enhancement is seen at small radius ratios ($r_{HST}/r_{MUSE} \lesssim 0.2$), possibly indicating an increased DIG contribution. However, the lowest-radius-ratio bin, where these deviations are most pronounced, contains relatively few sources, limiting its statistical significance.

To quantify the global impact, we find that from $r_{HST}/r_{MUSE} = 0.2$ to 0.8, the median binned values of [OIII]/Hβ, [NII]/Hα, [SII]/Hα, and [OI]/Hα differ from the global sample median by less than 25%. This suggests that DIG contamination does not systematically bias the diagnostic line ratios for the majority of sources in the MUSE nebular catalogue. We therefore conclude that, although DIG may locally affect the emission-line properties of compact, unresolved sources, its overall impact on the catalogue-wide line ratio distributions is limited. These findings support the reliability of the MUSE H II region catalogue, with minimal systematic bias introduced by unresolved DIG contamination.

6. Summary and outlook

We present the PHANGS-MUSE/HST-Hα nebulae catalogue, comprising 5177 spatially resolved ionised nebulae across 19 nearby galaxies ($D < 20$ Mpc), based on high-resolution HST narrow-band imaging homogenised to a uniform physical resolution and sensitivity. Combined with PHANGS-MUSE spectroscopy, this dataset enables robust classification of 4882 H II regions, as well as the identification and separation of planetary nebulae and supernova remnants.

Key physical properties, including sizes, electron densities, and ionising photon production rates, are derived for each region. A median H II region radius of ~20 pc is measured, with sizes extending down to the 10 pc resolution limit. We introduce a complexity score to quantify internal nebular substructure, revealing that approximately one-third of regions comprise morphologically complex H II complexes containing multiple clusters and bubbles, particularly in galaxy centres.

A luminosity–size relation is calibrated using the HST-resolved regions and applied to the full PHANGS-MUSE nebular catalogue, enabling the recovery of physical sizes down to ~1 pc and correcting for incompleteness in the HST catalogue. Observed nebular sizes systematically exceed those predicted by classical Strömgren sphere models, corresponding to typical volume filling factors with a median of $\epsilon \sim 0.22$ (10th–90th percentile 0.06–0.78). Compact ~10 pc regions approach unity, while progressively larger regions exhibit systematically lower filling factors, consistent with the clumpy, shell-dominated morphologies seen in resolved nebulae.

By associating nebulae with stellar populations from the PHANGS-HST catalogue, we find that most H II regions are powered by young (median age ~3 Myr) stellar populations with typical masses of 10^4–10^5 M$_\odot$. A positive correlation between

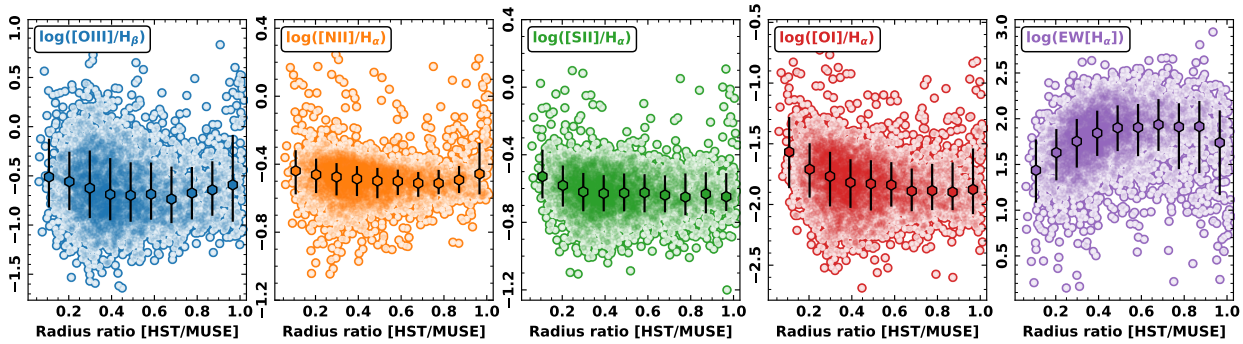

Fig. 14. Line ratio diagnostic diagrams and radius ratio $r_{\rm HST}/r_{\rm MUSE}$ analysis. Scatter plots of circular ($r_{\rm circ}$) radius ratios (HST/MUSE) versus various line diagnostics – [OIII]/Hβ, [NII]/Hα, [SII]/Hα, and [OI]/Hα – along with the equivalent width of Hα (in units of log(Å)). Overlaid are equally spaced binned points (median values of bins shown), with error bars indicating the standard deviation of the points within each bin.

region size and stellar mass is observed, consistent with expectations from photoionisation models. We find no significant systematic biases in nebular emission-line ratios due to unresolved diffuse ionised gas, supporting the reliability of MUSE spectroscopy for global diagnostic studies.

The PHANGS-MUSE/HST-Hα catalogue provides a comprehensive, spatially resolved view of ionised nebulae across a representative sample of nearby galaxies. This dataset enables detailed studies of nebular structure, feedback processes, and the connection between star formation and the interstellar medium. In future work, we aim to combine this catalogue with high-resolution data from JWST, ALMA, and other facilities to further characterise the multi-phase interstellar medium and the role of stellar feedback in shaping galaxy evolution.

The complete catalogue, including all 5467 nebulae and 241 measured columns, is made publicly available via CDS, together with a comprehensive README describing all columns. Associated products include region masks (with values corresponding to the `region_id` in the catalogue and matched to the PHANGS-MUSE catalogue of Groves et al. 2023) and the homogenised HST Hα maps convolved to 10 pc resolution that form the basis of this catalogue.

Data availability

The catalog is available at the CDS via `https://cdsarc.cds.unistra.fr/viz-bin/cat/J/A+A/706/A95`

Acknowledgements. ATB dedicates this paper to his wife, Christina Barnes, for beginning this new chapter as parents together, and warmly acknowledges their son, Theodore Michael Barnes, for graciously waiting two hours after its submission before beginning his entrance into the world. The authors of this paper are grateful to the anonymous referee for their constructive and detailed suggestions, which helped significantly improve the quality of this paper. This work has been carried out as part of the PHANGS collaboration. Based on observations from the PHANGS-MUSE programme, collected at the European Southern Observatory under ESO programmes 094.C-0623 (PI: Kreckel), 095.C-0473, 098.C-0484 (PI: Blanc), 1100.B-0651 (PHANGS-MUSE; PI: Schinnerer), as well as 094.B-0321 (MAGNUM; PI: Marconi), 099.B-0242, 0100.B-0116, 098.B-0551 (MAD; PI: Carollo) and 097.B-0640 (TIMER; PI: Gadotti). In addition, this research is based on observations made with the NASA/ESA Hubble Space Telescope obtained from the Space Telescope Science Institute, which is operated by the Association of Universities for Research in Astronomy, Inc., under NASA contract NAS 5–26555. These observations are associated with programmes 15654, 17126, and 17457. FB acknowledges support from the INAF Fundamental Astrophysics programme 2022. KK gratefully acknowledges funding from the Deutsche Forschungsgemeinschaft (DFG, German Research Foundation) in the form of an Emmy Noether Research Group (grant number KR4598/2-1, PI Kreckel) and the European Research Council's starting grant ERC StG-101077573 ("ISM-METALS"). SCOG and RSK acknowledge financial support from the European Research Council via the ERC Synergy Grant 'ECOGAL' (project ID 855130) and from the German Excellence Strategy via the Heidelberg Cluster of Excellence (EXC 2181 – 390900948) 'STRUCTURES'. KG is supported by the Australian Research Council through the Discovery Early Career Researcher Award (DECRA) Fellowship (project number DE220100766) funded by the Australian Government. OE acknowledges funding from the Deutsche Forschungsgemeinschaft (DFG, German Research Foundation) – project-ID 541068876. RSK also acknowledges support from the German Ministry for Economic Affairs and Climate Action in project 'MAINN' (funding ID 50OO2206). In addition, RSK thanks the 2024/25 Class of Radcliffe Fellows for highly interesting and stimulating discussions. ZB gratefully acknowledges the Collaborative Research Center 1601 (SFB 1601 sub-project B3) funded by the Deutsche Forschungsgemeinschaft (DFG, German Research Foundation) – 500700252. MB acknowledges support from the ANID BASAL project FB210003. This work was supported by the French government through the France 2030 investment plan managed by the National Research Agency (ANR), as part of the Initiative of Excellence of Université Côte d'Azur under reference number ANR-15-IDEX-01.

References

Anand, G. S., Lee, J. C., Van Dyk, S. D., et al. 2021a, MNRAS, 501, 3621
Anand, G. S., Rizzi, L., Tully, R. B., et al. 2021b, AJ, 162, 80
Anderson, L. D., Bania, T. M., Balser, D. S., et al. 2014, ApJS, 212, 1
Baldwin, J. A., Phillips, M. M., & Terlevich, R. 1981, PASP, 93, 5
Barnes, A. T., Glover, S. C. O., Kreckel, K., et al. 2021, MNRAS, 508, 5362
Barnes, A. T., Chandar, R., Kreckel, K., et al. 2022, A&A, 662, L6
Barnes, A. T., Watkins, E. J., Meidt, S. E., et al. 2023, ApJ, 944, L22
Boquien, M., Burgarella, D., Roehlly, Y., et al. 2019, A&A, 622, A103
Brazzini, M., Belfiore, F., Ginolfi, M., et al. 2024, A&A, 691, A173
Brown, G., & Gnedin, O. Y. 2021, MNRAS, 508, 5935
Bruzual, G., & Charlot, S. 2003, MNRAS, 344, 1000
Bryant, J. J., Owers, M. S., Robotham, A. S. G., et al. 2015, MNRAS, 447, 2857
Bundy, K., Bershady, M. A., Law, D. R., et al. 2015, ApJ, 798, 7
Byler, N., Dalcanton, J. J., Conroy, C., & Johnson, B. D. 2017, ApJ, 840, 44
Cedrés, B., Beckman, J. E., Bongiovanni, Á., et al. 2013, ApJ, 765, L24
Chabrier, G. 2003, PASP, 115, 763
Chandar, R., Barnes, A. T., Thilker, D. A., et al. 2025, AJ, 169, 150
Congiu, E., Blanc, G. A., Belfiore, F., et al. 2023, A&A, 672, A148
Della Bruna, L., Adamo, A., Bik, A., et al. 2020, A&A, 635, A134
Diaz, A. I., Terlevich, E., Vilchez, J. M., Pagel, B. E. J., & Edmunds, M. G. 1991, MNRAS, 253, 245
Dolphin, A. 2016, DOLPHOT: Stellar photometry, Astrophysics Source Code Library [record ascl:1608.013]
Draine, B. T. 2011, Physics of the Interstellar and Intergalactic Medium
Drory, N., Blanc, G. A., Kreckel, K., et al. 2024, AJ, 168, 198
Elmegreen, B. G., & Lada, C. J. 1977, ApJ, 214, 725
Emsellem, E., Schinnerer, E., Santoro, F., et al. 2022, A&A, 659, A191
Erroz-Ferrer, S., Carollo, C. M., den Brok, M., et al. 2019, MNRAS, 484, 5009
Ferland, G. J., Peterson, B. M., Horne, K., Welsh, W. F., & Nahar, S. N. 1992, ApJ, 387, 95
Fruchter, A. S., & Hook, R. N. 2002, PASP, 114, 144
Gadotti, D. A., Sánchez-Blázquez, P., Falcón-Barroso, J., et al. 2019, MNRAS, 482, 506
Grasha, K., Elmegreen, B. G., Calzetti, D., et al. 2017, ApJ, 842, 25
Grasha, K., Chen, Q. H., Battisti, A. J., et al. 2022, ApJ, 929, 118
Groves, B., Kreckel, K., Santoro, F., et al. 2023, MNRAS, 520, 4902
Haffner, L. M., Dettmar, R. J., Beckman, J. E., et al. 2009, Rev. Mod. Phys., 81, 969

Henny, K. F., Dale, D. A., Chandar, R., et al. 2025, ApJ, 991, 76
Ho, I. T., Seibert, M., Meidt, S. E., et al. 2017, ApJ, 846, 39
Hui, L., & Gnedin, N. Y. 1997, MNRAS, 292, 27
Kauffmann, G., Heckman, T. M., Tremonti, C., et al. 2003, MNRAS, 346, 1055
Kennicutt, Jr., R. C. 1984, ApJ, 287, 116
Kewley, L. J., Dopita, M. A., Sutherland, R. S., Heisler, C. A., & Trevena, J. 2001, ApJ, 556, 121
Kewley, L. J., Nicholls, D. C., & Sutherland, R. S. 2019, ARA&A, 57, 511
Kreckel, K., Ho, I. T., Blanc, G. A., et al. 2019, ApJ, 887, 80
Kreckel, K., Egorov, O. V., Egorova, E., et al. 2024, A&A, 689, A352
Kruskal, W. H., & Wallis, W. A. 1952, J. Am. Statist. Assoc., 47, 583
Lang, P., Meidt, S. E., Rosolowsky, E., et al. 2020, ApJ, 897, 122
Larson, K. L., Lee, J. C., Thilker, D. A., et al. 2023, MNRAS, 523, 6061
Lee, J. C., Whitmore, B. C., Thilker, D. A., et al. 2022, ApJS, 258, 10
Lee, J. C., Sandstrom, K. M., Leroy, A. K., et al. 2023, ApJ, 944, L17
Leitherer, C., Schaerer, D., Goldader, J. D., et al. 1999, ApJS, 123, 3
Li, J., Kreckel, K., Sarbadhicary, S., et al. 2024, A&A, 690, A161
Leroy, A. K., Sandstrom, K. M., Lang, D., et al. 2019, ApJS, 244, 24
Leroy, A. K., Schinnerer, E., Hughes, A., et al. 2021, ApJS, 257, 43
Lopez, L. A., Krumholz, M. R., Bolatto, A. D., Prochaska, J. X., & Ramirez-Ruiz, E. 2011, ApJ, 731, 91
Lopez, L. A., Krumholz, M. R., Bolatto, A. D., et al. 2014, ApJ, 795, 121
Luridiana, V., Morisset, C., & Shaw, R. A. 2015, A&A, 573, A42
Makarov, D., Prugniel, P., Terekhova, N., Courtois, H., & Vauglin, I. 2014, A&A, 570, A13
Maschmann, D., Lee, J. C., Thilker, D. A., et al. 2024, ApJS, 273, 14
McLeod, A. F., Dale, J. E., Evans, C. J., et al. 2019, MNRAS, 486, 5263
McLeod, A. F., Kruijssen, J. M. D., Weisz, D. R., et al. 2020, ApJ, 891, 25
McLeod, A. F., Ali, A. A., Chevance, M., et al. 2021, MNRAS, 508, 5425
Méndez-Delgado, J. E., Esteban, C., García-Rojas, J., et al. 2023, MNRAS, 523, 2952
Osterbrock, D., & Flather, E. 1959, ApJ, 129, 26
Osterbrock, D. E., & Ferland, G. J. 2006, Astrophysics of gaseous nebulae and active galactic nuclei (University Science Books)
Pathak, D., Leroy, A. K., Thompson, T. A., et al. 2025, ApJ, 982, 140
Pedrini, A., Adamo, A., Calzetti, D., et al. 2024, ApJ, 971, 32
Pilyugin, L. S., & Grebel, E. K. 2016, MNRAS, 457, 3678
Querejeta, M., Schinnerer, E., Meidt, S., et al. 2021, A&A, 656, A133
Relaño, M., & Kennicutt, Jr., R. C. 2009, ApJ, 699, 1125
Reynolds, R. J. 1990, ApJ, 349, L17
Rosolowsky, E., Hughes, A., Leroy, A. K., et al. 2021, MNRAS, 502, 1218
Rosolowsky, E., & Leroy, A. 2006, PASP, 118, 590
Rosolowsky, E. W., Pineda, J. E., Kauffmann, J., & Goodman, A. A. 2008, ApJ, 679, 1338
Rousseau-Nepton, L., Martin, R. P., Robert, C., et al. 2019, MNRAS, 489, 5530
Rynkun, P., Gaigalas, G., & Jönsson, P. 2019, A&A, 623, A155
Salo, H., Laurikainen, E., Laine, J., et al. 2015, ApJS, 219, 4
Sánchez, S. F., Kennicutt, R. C., Gil de Paz, A., et al. 2012, A&A, 538, A8
Sánchez, S. F., Lugo-Aranda, A. Z., Sánchez Almeida, J., et al. 2024, A&A, 682, A71
Santoro, F., Kreckel, K., Belfiore, F., et al. 2022, A&A, 658, A188
Scheuermann, F., Kreckel, K., Barnes, A. T., et al. 2023, MNRAS, 522, 2369
Schinnerer, E., & Leroy, A. K. 2024, ARA&A, 62, 369
Storey, P. J., & Hummer, D. G. 1995, MNRAS, 272, 41
Strömgren, B. 1939, ApJ, 89, 526
Tayal, S. S., & Zatsarinny, O. 2010, ApJS, 188, 32
Thilker, D. A., Braun, R., & Walterbos, R. A. M. 2000, AJ, 120, 3070
Thilker, D. A., Lee, J. C., Whitmore, B. C., et al. 2025, ApJS, 280, 1
van der Walt, S., Schönberger, J. L., Nunez-Iglesias, J., et al. 2014, PeerJ, 2, e453
van de Sande, J., Fraser-McKelvie, A., Fisher, D. B., et al. 2024, in IAU Symposium, 377, Early Disk-Galaxy Formation from JWST to the Milky Way, eds. F. Tabatabaei, B. Barbuy, & Y.-S. Ting, 27
Walborn, N. R., & Parker, J. W. 1992, ApJ, 399, L87
Walborn, N. R., & Blades, J. C. 1997, ApJS, 112, 457
Watkins, E. J., Barnes, A. T., Henny, K., et al. 2023a, ApJ, 944, L24
Watkins, E. J., Kreckel, K., Groves, B., et al. 2023b, A&A, 676, A67
Weilbacher, P. M., Monreal-Ibero, A., Kollatschny, W., et al. 2015, A&A, 582, A114
Whitmore, B. C., Chandar, R., Schweizer, F., et al. 2010, AJ, 140, 75
Whitmore, B. C., Chandar, R., Lee, J. C., et al. 2025, ApJ, 982, 50
Williams, T. G., Lee, J. C., Larson, K. L., et al. 2024, ApJS, 273, 13

[1] European Southern Observatory (ESO), Karl-Schwarzschild-Straße 2, 85748 Garching, Germany
[2] Ritter Astrophysical Research Center, University of Toledo, Toledo, OH 43606, USA
[3] Department of Physics and Astronomy, The Johns Hopkins University, Baltimore, MD 21218, USA
[4] Astronomisches Rechen-Institut, Zentrum für Astronomie der Universität Heidelberg, Mönchhofstraße 12–14, 69120 Heidelberg, Germany
[5] INAF — Osservatorio Astrofisico di Arcetri, Largo E. Fermi 5, 50125 Florence, Italy
[6] International Centre for Radio Astronomy Research, University of Western Australia, 7 Fairway, Crawley, 6009 WA, Australia
[7] Universität Heidelberg, Zentrum für Astronomie, Institut für Theoretische Astrophysik, Albert-Ueberle-Str. 2, 69120 Heidelberg, Germany
[8] Department of Astronomy, Ohio State University, 180 W. 18th Ave, Columbus, OH 43210, USA
[9] Center for Cosmology and Astroparticle Physics, 191 West Woodruff Avenue, Columbus, OH 43210, USA
[10] Space Telescope Science Institute, 3700 San Martin Drive, Baltimore, MD 21218, USA
[11] Research School of Astronomy and Astrophysics, Australian National University, Canberra, ACT 2611, Australia
[12] Sub-department of Astrophysics, Department of Physics, University of Oxford, Keble Road, Oxford OX1 3RH, UK
[13] Department of Physics & Astronomy, University of Wyoming, Laramie, WY 82071, USA
[14] European Southern Observatory (ESO), Alonso de Córdova 3107, Casilla 19, Santiago 19001, Chile
[15] Instituto de Astronomía, Universidad Nacional Autónoma de México, Ap. 70-264, 04510 CDMX, Mexico
[16] Observatorio Astronómico Nacional (IGN), C/ Alfonso XII 3, 28014 Madrid, Spain
[17] Sterrenkundig Observatorium, Universiteit Gent, Krijgslaan 281 S9, 9000 Gent, Belgium
[18] Argelander-Institut für Astronomie, University of Bonn, Auf dem Hügel 71, 53121 Bonn, Germany
[19] Instituto de Astronomía, Universidad Nacional Autónoma de México, Unidad Académica en Ensenada, Km 103 Carr. Tijuana-Ensenada, Ensenada, BC, Mexico
[20] Université Côte d'Azur, Observatoire de la Côte d'Azur, CNRS, Laboratoire Lagrange, 06000 Nice, France
[21] Astronomy Department, University of Virginia, PO Box 400325, Charlottesville, VA 22904, USA
[22] National Radio Astronomy Observatory, 520 Edgemont Rd, Charlottesville, VA 22903, USA
[23] Department of Physics, University of Arkansas, 226 Physics Building, 825 West Dickson Street, Fayetteville, AR 72701, USA
[24] Max-Planck-Institut für Astronomie, Königstuhl 17, 69117 Heidelberg, Germany
[25] Department of Physics, Tamkang University, No.151, Yingzhuan Road, Tamsui District, New Taipei City 251301, Taiwan
[26] Steward Observatory, University of Arizona, Tucson, AZ 85721, USA
[27] Gemini Observatory/NSF's NOIRLab, 950 N. Cherry Avenue, Tucson, AZ 85719, USA
[28] Department of Physics, 4-183 CCIS, University of Alberta, Edmonton, AB T6G 2E1, Canada

Appendix A: Nebula catalogue

The PHANGS-HST Hα Nebulae Catalogue (DR1) provides a homogeneous set of measurements for 5467 regions (i.e. without any flag-based filtering) identified across the 19 nearby galaxies in the PHANGS-HST sample. Each catalogue entry corresponds to a single nebula, with positions, sizes, fluxes, luminosities, and a variety of derived physical parameters. These include electron densities, ionisation parameters, and metallicities from matched PHANGS-MUSE spectroscopy, as well as stellar association ages and masses from the PHANGS-HST multi-scale stellar association catalogues.

Table A.1 illustrates a representative subset of the catalogue, showing a few rows and a selection of columns. The full catalogue contains 241 columns, spanning structural, photometric, spectroscopic, and environmental properties. A complete description of all parameters included in the table is provided in Table A.2 and A.3. The catalogue itself, including the full sample of 5467 regions, together with the complete documentation, is accessible online via CDS.

Appendix B: Galaxy sample

Table B.1 provides an overview of the properties of the 19 galaxies included in this study.

Appendix C: Maps

Figure C.1 show additional example nebulae exhibiting simple, intermediate, and complex morphologies.

Appendix D: Luminosity distributions and flux recovery

In Fig. D.1, we present the Hα luminosity distributions for all regions in the PHANGS-MUSE/HST-Hα nebula catalogue. When comparing the subset of sources matched between the HST and MUSE catalogues, we find that both distributions peak at similar luminosities in the range $L_{\mathrm{H}\alpha} \sim 10^{37}$–$10^{38}$ erg s^{-1}, with a systematic offset in the median luminosity of approximately a factor of two (see lower panel of Fig. D.1)[9].

Given that the HST observations are both lower in sensitivity and can detect more compact structures than MUSE, we do not expect the HST catalogue to recover the full Hα flux for most regions. Nonetheless, we find that a small fraction (48) of regions exhibit $L_{\mathrm{H}\alpha}$(HST) significantly (50%) higher than $L_{\mathrm{H}\alpha}$(MUSE) (see inset in Fig. D.1), which, are limited to known problematic regions (e.g. centres or particularly complex regions).

In Fig. D.2, we show the ratio r_{circ}(HST)/r_{circ}(MUSE) as a function of r_{circ}(HST), r_{circ}(MUSE), $L_{\mathrm{H}\alpha}$(HST), and $L_{\mathrm{H}\alpha}$(HST)/$L_{\mathrm{H}\alpha}$(MUSE). As expected, larger HST regions are more comparable in size to their MUSE counterparts. Moreover, we find that the larger and more luminous nebulae are those for which a higher fraction of the total MUSE flux is recovered in the HST data. The final panel shows that regions with more similar sizes between HST and MUSE also exhibit more similar Hα luminosities, indicating that spatially extended regions are better matched across both catalogues.

[9] This comparison includes only regions that are identified in both the HST and MUSE catalogues. For the full luminosity distribution of all MUSE regions, see Fig. 3.

Appendix E: Size-Luminosity distributions

Figure E.1 presents the distribution of Hα luminosity ratios between HST and MUSE detections, separated by galactic environment (i.e. centre, bar, arm, interarm, and disc regions). The histograms and cumulative distributions indicate that MUSE captures a larger fraction of the total luminosity in central environment, while arm, bar and interarm regions show comparatively lower recovery fractions. This trend reflects underlying environmental differences in gas density, feedback, and star formation structure. These results are consistent with the result that larger, more complex regions (which tend to reside in centres) recover more total flux.

The cumulative distributions confirm that HST observations capture a significant fraction of the Hα emission, particularly from smaller and denser nebulae missed in lower-resolution datasets.

Appendix F: Size distribution as function of environment

In Fig. F.1, we show the size distributions as a function of environment.

Appendix G: BPT ratios as a function of luminosity

As discussed in Sect. 5.4, we assess the impact of diffuse ionised gas (DIG) on nebular line ratios. In Fig. G.1, we reproduce the panels from Fig. 14 but substitute the x-axis with the ratio of the Hα luminosities measured with HST and MUSE. This provides an alternative view of how DIG-related dilution may influence diagnostic line ratios.

Appendix H: Nebulae and stellar properties

Table H.1 summarises the statistics of nebular radii and luminosities for each galaxy in the catalogue. Table H.3 provides the corresponding stellar properties for matched associations, including their masses and ages.

Appendix I: Data homogenisation

In order to compare nebular properties across the PHANGS sample, all HST Hα images were homogenised to a common physical resolution of 10 pc by convolution with a Gaussian kernel. The applied noise contribution is computed as

$$\sigma^2_{\mathrm{applied,10pc}} = \sigma^2_{\mathrm{final,10pc}} - \sigma^2_{\mathrm{obs,10pc}}, \tag{I.1}$$

where $\sigma_{\mathrm{obs,10pc}}$ is the median noise level measured in the 10 pc-smoothed image.

Several caveats should be noted (see Lee et al. 2022; Chandar et al. 2025 for more details on the specific data reduction for PHANGS-HST). First, the noise properties of HST data products differ from the Gaussian assumption adopted here. Photon-counting statistics yield an intrinsically Poissonian noise distribution, and the drizzling process used to combine dithered exposures introduces correlated noise between neighbouring pixels. As shown by Fruchter & Hook (2002), the correlation arises because input pixels are resampled onto the output grid with fractional overlaps, so that the pixel-to-pixel RMS underestimates the true noise on larger spatial scales.

Second, the HST PSF is not well described by a Gaussian, exhibiting diffraction features and Airy rings. In addition, the

Table A.1. Example entries from the PHANGS-HST Hα Nebulae Catalogue.

galaxy_name	region_ID	ra	dec	radius_circ_pc	halpha_flux	ne_sii_muse	age_assoc_nuv_08pc	mass_assoc_nuv_08pc	...
		°	°	pc	erg s^{-1} cm^{-2}	cm^{-3}	Myr	M$_\odot$	...
IC5332	7.0	353.606	-36.115	11.88	8.07e-16	57.52			...
IC5332	17.0	353.632	-36.087	18.73	2.05e-15	37.12			...
IC5332	26.0	353.601	-36.107	27.57	8.01e-15	85.32			...
IC5332	28.0	353.608	-36.112	16.04	1.34e-15				...
IC5332	29.0	353.623	-36.089	16.80	1.22e-15		3.00	685.84	...
IC5332	31.0	353.595	-36.084	18.96	2.65e-15	48.27	2.00	2947.84	...
IC5332	33.0	353.616	-36.103	9.05	3.94e-16				...
IC5332	55.0	353.629	-36.096	30.64	3.52e-15				...
IC5332	57.0	353.615	-36.096	16.04	1.16e-15	73.19			...
IC5332	60.0	353.614	-36.103	19.38	1.69e-15		3.00	811.32	...
IC5332	82.0	353.615	-36.106	27.20	2.84e-15		1.00	4344.19	...
IC5332	84.0	353.603	-36.114	31.34	5.68e-15	34.76	4.00	187.42	...
IC5332	91.0	353.605	-36.104	10.74	7.08e-14				...
IC5332	92.0	353.598	-36.094	27.46	3.17e-15		1.00	1667.13	...
IC5332	108.0	353.616	-36.097	19.26	1.4e-15				...
IC5332	125.0	353.611	-36.082	19.38	1.72e-15				...
IC5332	127.0	353.609	-36.090	14.35	9.14e-16				...
IC5332	129.0	353.616	-36.099	9.42	6.04e-16	60.09			...
IC5332	141.0	353.612	-36.111	47.20	1.71e-14	40.51	3.00	160.10	...
IC5332	153.0	353.627	-36.104	13.21	7.63e-16				...
...	...	...	...	...	...	...	...	...	...

Notes. We show a truncated subset of the full catalogue, including only the first rows for IC 5332 and a small selection of columns. Displayed parameters include the galaxy name, region identifier, J2000 right ascension and declination of the region centroid, circularised radius (pc), Hα flux measured from HST imaging, electron density from the [S II] λ6716/λ6731 ratio measured with PHANGS-MUSE, and age and stellar mass of the nearest NUV-selected stellar association at the 8 pc scale (Larson et al. 2023). The full catalogue contains 5467 entries across 19 galaxies, with 245 columns providing coordinates, sizes, fluxes, luminosities, morphologies, derived physical parameters, and cross-matched stellar association properties. The complete version of this table is available online at CDS.

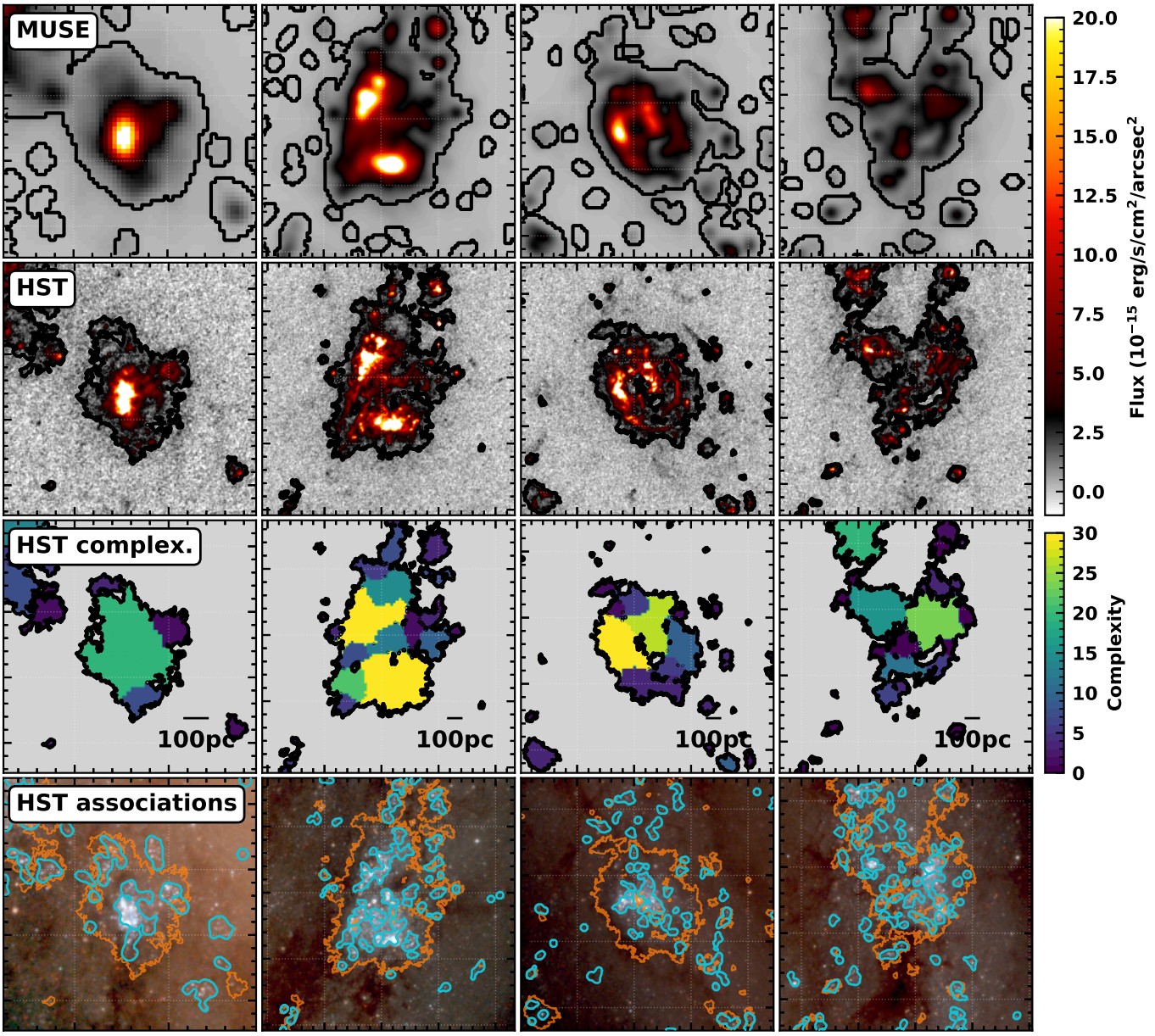

Fig. C.1. Example of several regions within the nebula catalogues towards NGC 1566. The MUSE (*first row*) and HST (*second row*) observations, overlaid with contours showing the boundary of each source in the respective observations. (*third row*) We show a map of the complexity score for each region. (*fourth row*) We show the nebula (red contours) and 32 pc NUV-identified stellar association (Larson et al. 2023; blue contour) overlaid on a HST filter red (F814W) green (F555W) blue (F438W+F336W) image (see Lee et al. 2022).

PSF varies across the detector field of view, meaning that the effective shape is not spatially invariant. The drizzling process used to combine dithered exposures further modifies the PSF, with the exact outcome depending on the chosen kernel and pixel fraction parameters, typically broadening the core and altering the wings.

Finally, the images contain a mix of correlated and uncorrelated components due to both the detector sampling and the drizzling resampling. While a Gaussian kernel provides a convenient first-order approximation for homogenisation, it cannot perfectly capture these subtleties. Nonetheless, adopting a common Gaussian PSF of 10 pc allows for consistent comparison across the sample, and we emphasise that the small deviations introduced by this simplification do not affect our primary conclusions. Future work may incorporate more sophisticated homogenisation schemes that explicitly propagate correlated noise and non-Gaussian PSF structure.

Fig. I.1 illustrates the impact of smoothing and noise rescaling for two representative galaxies: NGC 1300 (upper panels) and NGC 5068 (lower panels). NGC 1300, one of the most distant galaxies in the sample (18.99 Mpc; Anand et al. 2021b,a), has relatively low intrinsic noise and therefore requires little smoothing but a significant amount of additional noise injection. In contrast, NGC 5068 is among the nearest galaxies (5.20 Mpc; Anand et al. 2021b,a), requiring substantial smoothing and added noise. For each galaxy we show the noise distributions of the native image, the image smoothed to 10 pc resolution, and the smoothed image with added noise. Gaussian fits to the distributions are overplotted to highlight the similarities and differences. The native images show clear deviations from Gaussian behaviour, with extended tails towards negative values as

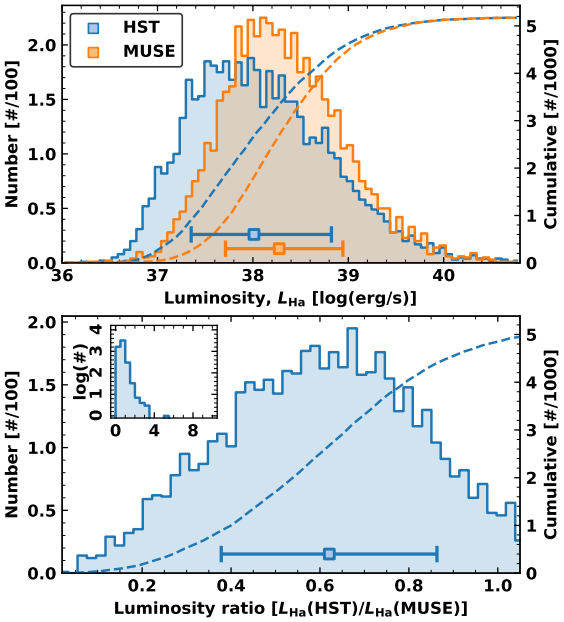

Fig. D.1. Distribution of source luminosities for all regions in the Nebula Catalogues. In blue and orange we show the distribution for sources identified in both the HST and MUSE observations. Note that we only show the MUSE sample that was also identified by HST (i.e. not the full sample identified by Groves et al. 2023). The inset axis shows a larger range in luminosity ratios, and is shown in a log distribution for clarity. In contrast to Fig. 4, this shows that despite the regions being much smaller in the HST observations, they still typically retain a significant fraction of the flux.

expected for Poisson statistics (noting that the positive tail may also include contamination from real emission). The smoothed images also deviate from purely Gaussian profiles, though in the case of NGC 5068 the smoothing strongly reduces the effective noise level (but not for NGC 1300). Finally, adding noise back in produces images with noise properties more consistent across the sample. While this procedure is not ideal for the reasons discussed above, it provides a practical and uniform approach, which can be improved upon in future work.

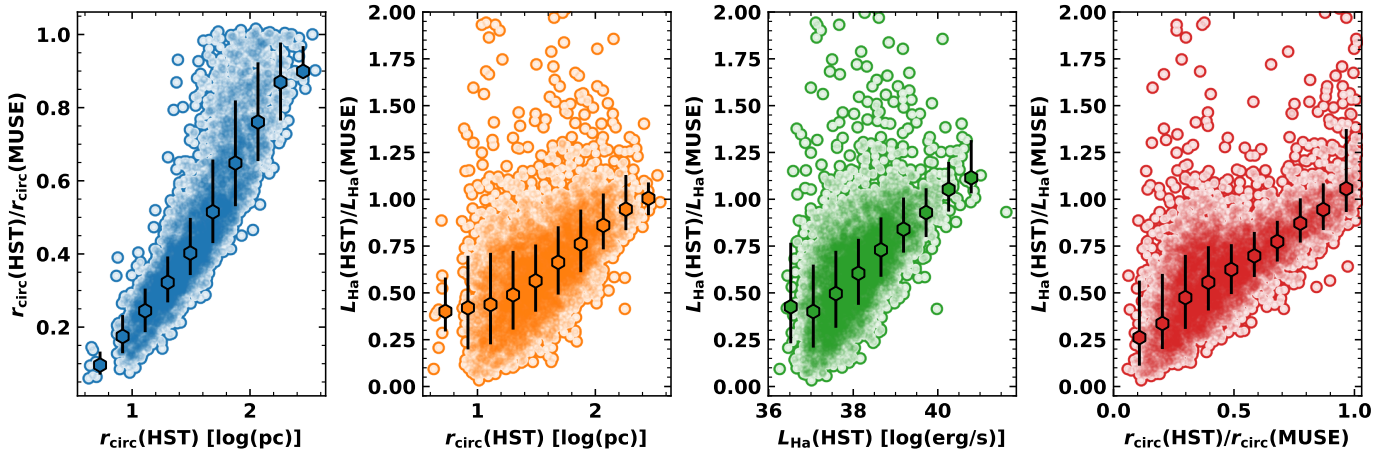

Fig. D.2. Distribution of sizes and luminosities. (*First panel*) We show the ratio of r_{circ}(HST)/r_{circ}(MUSE) as a function of the HST sizes (r_{circ}(HST)). (*Second panel*) We show the luminosity ratio $L_{H\alpha}$(HST)/$L_{H\alpha}$(MUSE) as a function of the HST sizes (r_{circ}(HST)). (Third panel) We show the luminosity ratio as a function of the HST luminosity, $L_{H\alpha}$(HST). (Fourth panel) We show the luminosity ratio as a function of the radius ratio. Overlaid on all panels are equally spaced binned points (median values of bins shown), with error bars indicating the standard deviation of the points within each bin.

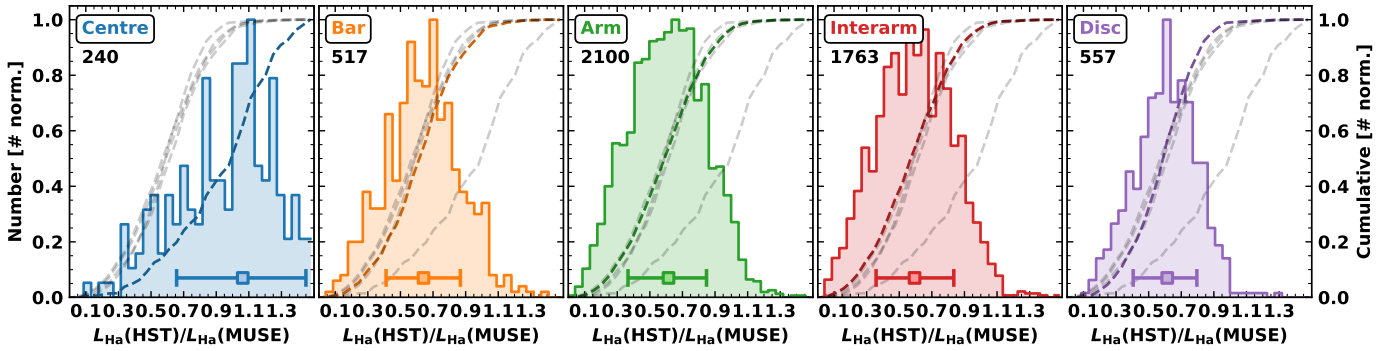

Fig. E.1. Distribution of source luminosities ratios (HST/MUSE) in the nebula catalogue within each environment (Querejeta et al. 2021). The ratio of the luminosities of each region identified in both the HST or MUSE observations (see lower panel of Fig. D.1 for full distribution). We show the histogram and cumulative distributions as solid filled and dashed lines, respectively. For comparison, all distributions are normalised to unity, and overlaid on each panel as light dashed grey lines are the cumulative distributions from the other panels.

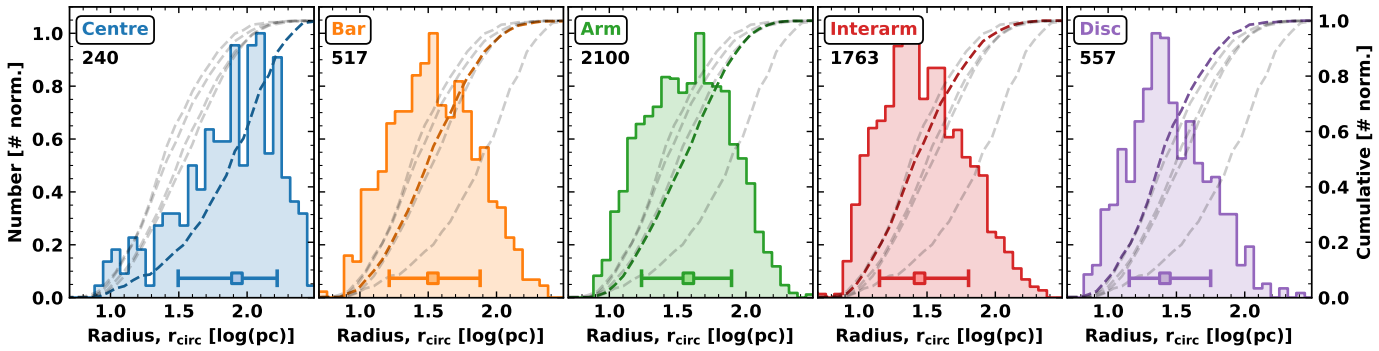

Fig. F.1. Distribution of source sizes in the nebula catalogue within each environment (Querejeta et al. 2021). We show the histogram and cumulative distributions as solid filled and dashed lines, respectively (see upper left number of regions in each histogram). For comparison, all distributions are normalised to unity, and overlaid on each panel as light dashed grey lines are the cumulative distributions from the other panels.

Table A.2. Description of selected columns from the PHANGS-MUSE/HST Hα Nebulae Catalogue (part I).

Column	Description
galaxy_name	Galaxy name
region_ID	Region identifier
flag_edge_hst	Flag=1 if region lies on HST image edge
flag_touch_hst	Flag=1 if region touches segmentation boundary
flag_manual_hst	Manual classification flags (visual checks)
flag_edge_muse	Flag=1 if region lies on MUSE cube edge
flag_star_muse	Flag=1 if affected by bright star in MUSE data
ra	Right ascension (J2000) of region centroid
dec	Declination (J2000) of region centroid
ra_peak	Right ascension (J2000) of Hα peak pixel
dec_peak	Declination (J2000) of Hα peak pixel
ra_muse	Right ascension (J2000) of MUSE centroid
dec_muse	Declination (J2000) of MUSE centroid
r_R25_deproj	Deprojected galactocentric radius, in R25 units
r_reff_deproj	Deprojected galactocentric radius, in Re units
phi_deproj	Deprojected azimuthal angle within host galaxy
environment	Environment flag following Querejeta et al. (2021)
area_circ_arcsec2	Circularised area (arcsec^2)
radius_circ_arcsec	Circularised radius (arcsec)
radius_circ_pc	Circularised radius (pc)
area_mom_arcsec2	Second-moment area of region (arcsec^2)
radius_major_mom_arcsec	Second-moment major axis (arcsec)
radius_minor_mom_arcsec	Second-moment minor axis (arcsec)
radius_pos_angle_deg	Position angle (moments-based)
radius_mom_arcsec	Moment-based radius (arcsec)
radius_mom_pc	Moment-based radius (pc)
radius_mom_deconv_pc	Deconvolved moment-based radius (pc)
radius_stromgren_pc	Stromgren radius (pc)
radius_circ_pc_muse	Circularised radius (pc; PHANGS-MUSE)
complexity_score	Morphological complexity score
halpha_flux	HST Hα integrated flux (raw, uncorrected)
halpha_flux_err	Error on HST Hα flux
halpha_flux_max	Maximum pixel flux in HST Hα map
halpha_flux_min	Minimum pixel flux in HST Hα map
halpha_flux_mean	Mean pixel flux in HST Hα map
halpha_flux_corr	Extinction-corrected HST Hα flux
halpha_flux_corr_err	Error on extinction-corrected HST Hα flux
<line>_flux_muse	Measured emission-line flux (PHANGS-MUSE)
<line>_flux_err_muse	Statistical uncertainty on flux (PHANGS-MUSE)
<line>_flux_corr_muse	Extinction-corrected flux (PHANGS-MUSE)
<line>_flux_corr_err_muse	Uncertainty on corrected flux (PHANGS-MUSE)
<line>_vel_muse	Velocity of <line> (PHANGS-MUSE)
<line>_vel_err_muse	Uncertainty on velocity of <line> (PHANGS-MUSE)
<line>_sigma_muse	Velocity dispersion of <line> (PHANGS-MUSE)
<line>_sigma_err_muse	Uncertainty on velocity dispersion of <line> (PHANGS-MUSE)
<line>_ew_muse	Equivalent width of <line> (Å; PHANGS-MUSE)
<line>_ew_err_muse	Uncertainty on equivalent width of <line> (Å; PHANGS-MUSE)
<line>_ew_<method>_muse	Equivalent width of <line> using <method> (Å; PHANGS-MUSE)
<line>_ew_<method>_err_muse	Uncertainty on equivalent width of <line> using <method> (Å; PHANGS-MUSE)

Notes. This table lists structural, positional, and spectroscopic parameters, including fluxes, velocities, dispersions, and equivalent widths. The parameters correspond to those shown in the example catalogue entries in Table A.1. Here <line> denotes an emission line (e.g. halpha, hbeta, oiii5007, nii6584, sii6716, sii6731, siii9069, oi6300, nii5755, hei5876, siii6312, oi6363, oii7319, oii7330). All fluxes are in erg s^{-1} cm^{-2}; velocities and dispersions are in km s^{-1}; equivalent widths are in Å. The suffix _err indicates 1σ statistical uncertainties; _corr indicates extinction-corrected values. The suffixes _vel and _sigma give line-of-sight velocity and velocity dispersion, respectively. EW variants use _raw (direct from the spectrum), _fit (from a fitted continuum/emission model), and _bgcorr (background-corrected). HST-specific columns halpha_flux_max, _min, and _mean are pixel statistics from the HST Hα map; halpha_flux_corr and _corr_err are extinction-corrected flux and its uncertainty.

Table A.3. Description of selected columns from the PHANGS-MUSE/HST Hα Nebulae Catalogue (part II, continued).

Column	Description
bpt_nii_muse	BPT class using [N II]/Hα (PHANGS-MUSE)
bpt_sii_muse	BPT class using [S II]/Hα (PHANGS-MUSE)
bpt_oi_muse	BPT class using [O I]/Hα (PHANGS-MUSE)
halpha_lum	Hα luminosity from HST (erg/s)
halpha_lum_err	Uncertainty on HST Hα luminosity (erg/s)
halpha_lum_muse	Hα luminosity from PHANGS-MUSE (erg/s; PHANGS-MUSE)
hii_class_v2_muse	PHANGS-MUSE H II classification (v2; PHANGS-MUSE)
hii_class_v3_muse	PHANGS-MUSE H II classification (v3; PHANGS-MUSE)
te_nii_muse	Electron temperature from [N II] (K; PHANGS-MUSE)
te_nii_err_muse	Uncertainty on Te([N II]) (K; PHANGS-MUSE)
te_siii_muse	Electron temperature from [S III] (K; PHANGS-MUSE)
te_siii_err_muse	Uncertainty on Te([S III]) (K; PHANGS-MUSE)
ne_sii_muse	Electron density from [S II] 6716/6731 (cm^{-3}; PHANGS-MUSE)
ne_sii_err_muse	Uncertainty on ne([S II]) (cm^{-3}; PHANGS-MUSE)
q	Ionizing photon rate Q (s^{-1})
q_err	Uncertainty on Q (s^{-1})
logq_d91_muse	log10(ionization parameter) (PHANGS-MUSE)
logq_d91_err_muse	Uncertainty on log10(ionization parameter) (PHANGS-MUSE)
ebv_muse	Colour excess E(B-V) from Balmer decrement (mag; PHANGS-MUSE)
ebv_err_muse	Uncertainty on E(B-V) (mag; PHANGS-MUSE)
av_muse	Visual extinction A_V (mag; PHANGS-MUSE)
metallicity_scal_muse	Gas-phase metallicity (Scal code; PHANGS-MUSE)
metallicity_scal_err_muse	Uncertainty on metallicity (Scal; PHANGS-MUSE)
metallicity_scal_delta_muse	Offset from local metallicity trend (dex; PHANGS-MUSE)
age_assoc_<filter>_<scale>	Stellar association age (Myr; PHANGS-HST)
age_err_assoc_<filter>_<scale>	Uncertainty on association age (Myr; PHANGS-HST)
ra_assoc_<filter>_<scale>	Association right ascension (deg; PHANGS-HST)
dec_assoc_<filter>_<scale>	Association declination (deg; PHANGS-HST)
ebv_assoc_<filter>_<scale>	Colour excess E(B–V) (mag; PHANGS-HST)
ebv_err_assoc_<filter>_<scale>	Uncertainty on E(B–V) (mag; PHANGS-HST)
mass_assoc_<filter>_<scale>	Stellar mass ($M_\odot$; PHANGS-HST)
mass_err_assoc_<filter>_<scale>	Uncertainty on stellar mass ($M_\odot$; PHANGS-HST)
region_ID_assoc_<filter>_<scale>	Association identifier (PHANGS-HST)
flag_multi_assoc_<filter>_<scale>	Flag: multiple matched associations (PHANGS-HST)
flag_one_assoc_<filter>_<scale>	Flag: exactly one matched association (PHANGS-HST)
flag_none_assoc_<filter>_<scale>	Flag: no matched association (PHANGS-HST)

Notes. This table provides additional parameters, including luminosities, physical conditions, ionisation properties, and stellar association matches. Together with Table A.2, this forms a full overview of the catalogue description. Columns related to stellar associations follow a repeated naming pattern. The format is <quantity>_assoc_<filter>_<scale>, where <filter> indicates the photometric band used for association identification (nuv = near-ultraviolet; v = optical V-band), and <scale> specifies the physical association scale in parsecs (08pc, 16pc, 32pc, 64pc). For example, age_assoc_nuv_08pc denotes the age of the stellar association identified in the NUV at an 8 pc scale, while mass_assoc_v_32pc would give the stellar mass of the V-band association at a 32 pc scale.

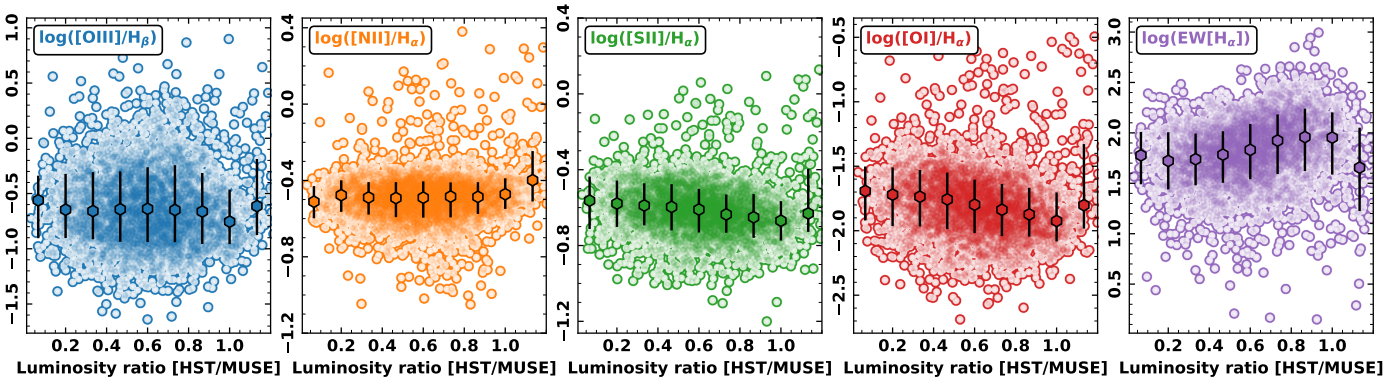

Fig. G.1. Line ratio diagnostic diagrams and luminosity ratio analysis. Scatter plots of circular ($r_{\rm circ}$) radius ratios (HST/MUSE) versus various line diagnostics – [OIII]/Hβ, [NII]/Hα, [SII]/Hα, and [OI]/Hα – along with the equivalent width of Hα (in units of log(Å)). Overlaid are equally spaced binned points (median values of bins shown), with error bars indicating the standard deviation of the points within each bin.

Table B.1. Properties of the galaxy sample.

Galaxy	i ° (a)	PA ° (a)	Morph. (b)	Dist. Mpc (c)	$R_{\rm eff}$ kpc (d)	Metal. 12+log(O/H) (e)	$M_{\rm HI}$ log($M_\odot$) (f)	$M_{\rm H_2}$ log($M_\odot$) (g)	$M_\star$ log($M_\odot$) (h)	SFR log($M_\odot$ yr^{-1}) (h)
IC 5332	26.9	74.4	SABc	9.0	3.6	8.37	9.3	–	9.7	-0.4
NGC 0628*	8.9	20.7	Sc	9.8	3.9	8.48	9.7	9.4	10.3	0.2
NGC 1087	42.9	359.1	Sc	15.9	3.2	8.40	9.1	9.2	9.9	0.1
NGC 1300	31.8	278.0	Sbc	19.0	6.5	8.52	9.4	9.4	10.6	0.1
NGC 1365	55.4	201.1	Sb	19.6	2.8	8.53	9.9	10.3	11.0	1.2
NGC 1385	44.0	181.3	Sc	17.2	3.4	8.42	9.2	9.2	10.0	0.3
NGC 1433	28.6	199.7	SBa	18.6	4.3	8.54	9.4	9.3	10.9	0.1
NGC 1512	42.5	261.9	Sa	18.8	4.8	8.55	9.9	9.1	10.7	0.1
NGC 1566	29.5	214.7	SABb	17.7	3.2	8.55	9.8	9.7	10.8	0.7
NGC 1672	42.6	134.3	Sb	19.4	3.4	8.54	10.2	9.9	10.7	0.9
NGC 2835	41.3	1.0	Sc	12.2	3.3	8.38	9.5	8.8	10.0	0.1
NGC 3351	45.1	193.2	Sb	10.0	3.0	8.59	8.9	9.1	10.4	0.1
NGC 3627	57.3	173.1	Sb	11.3	3.6	8.55	9.1	9.8	10.8	0.6
NGC 4254	34.4	68.1	Sc	13.1	2.4	8.53	9.5	9.9	10.4	0.5
NGC 4303	23.5	312.4	Sbc	17.0	3.4	8.56	9.7	9.9	10.5	0.7
NGC 4321	38.5	156.2	SABb	15.2	5.5	8.56	9.4	9.9	10.7	0.6
NGC 4535	44.7	179.7	Sc	15.8	6.3	8.54	9.6	9.6	10.5	0.3
NGC 5068	35.7	342.4	Sc	5.2	2.0	8.30	8.8	8.4	9.4	-0.6
NGC 7496	35.9	193.7	Sb	18.7	3.8	8.49	9.1	9.3	10.0	0.4

Notes. We show in columns from left to right the galaxy name, inclination (i), position angle (PA), morphological type (Morph.), distance (Dist.), effective radius ($R_{\rm eff}$), globally averaged metallicity (12 + log(O/H)), total mass of atomic gas ($M_{\rm HI}$), molecular gas ($M_{\rm H_2}$) and stars ($M_\star$), and global star formation rate (SFR). *We only make use of the archival "central" pointing observed with the F658N ACS HST filter, due to the lack of cross-over between the MUSE and newer F658N WFC3 HST filter "east" pointing (see Chandar et al. 2025). (*a*) From Lang et al. (2020), based on PHANGS CO(2–1) kinematics. For IC 5332, we use values from Salo et al. (2015). (*b*) Morphological classification taken from HyperLEDA (Makarov et al. 2014). (*c*) Source distances are taken from the compilation of Anand et al. (2021b,a). (*d*) $R_{\rm eff}$ that contains half of the stellar mass of the galaxy (Leroy et al. 2021). (*e*) Averaged metallicity within the area mapped by MUSE, computed using the Scal method of Pilyugin & Grebel (2016); see Kreckel et al. (2019) for more details. (*f*) Total atomic gas mass taken from HYPERLEDA (Makarov et al. 2014). (*g*) Molecular gas mass determined from PHANGS CO(2–1) observations (see Leroy et al. 2021). CO was not detected at high enough significance in IC 5332 to allow a molecular gas mass to be determined. (*h*) Derived by Leroy et al. (2021), using *GALEX* UV and *WISE* IR photometry, following a similar methodology to Leroy et al. (2019).

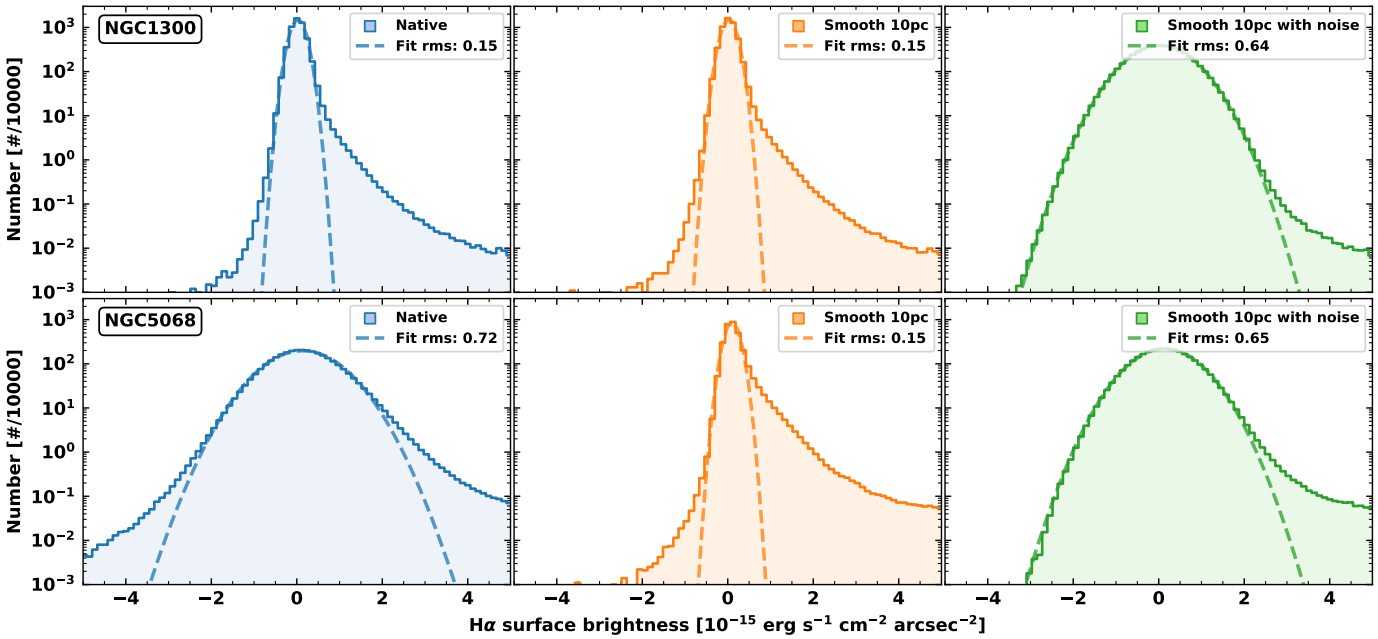

Fig. I.1. Pixel-value distributions of Hα surface brightness for two representative galaxies. Shown are histograms of the HST Hα images for NGC 1300 (upper panels) and NGC 5068 (lower panels), comparing the native data (left), the data convolved to a fixed physical resolution of 10 pc (middle), and the convolved data with additional noise added (right). Histograms are plotted as step lines with shaded areas, and Gaussian fits to the pixel distributions are overlaid as dashed curves. The fit standard deviation – approximately equivalent to the rms noise level of the image – is given in the legend of each panel in units of 10^{-15} erg s^{-1} cm^{-2} arcsec^{-2}.

Table H.1. Distribution of attenuation-corrected Hα luminosities and characteristic radii for each galaxy.

Galaxy	$L_{H\alpha}$ (HST) [log(erg s^{-1})]			$L_{H\alpha}$ (MUSE) [log(erg s^{-1})]			r_{circ} (HST) [pc]			r_{mom} (HST) [pc]			$r_{mom,deconv}$ (HST) [pc]			r_{str} [pc]			r_{circ} (MUSE) [pc]		
	10%	50%	90%	10%	50%	90%	10%	50%	90%	10%	50%	90%	10%	50%	90%	10%	50%	90%	10%	50%	90%
IC 5332	36.9	37.4	38.0	37.1	37.7	38.2	11.1	21.0	38.2	5.3	9.7	19.4	5.1	8.9	19.2	4.1	7.2	16.5	46.0	59.1	80.7
NGC 0628	37.1	37.6	38.4	37.3	37.9	38.6	11.6	21.8	47.6	5.1	10.4	23.7	3.8	9.8	23.8	6.2	13.0	22.0	40.4	60.7	95.4
NGC 1087	37.2	38.0	39.0	37.6	38.2	39.1	15.1	34.2	85.8	7.2	16.5	42.7	6.0	16.1	42.5	8.7	21.9	33.9	52.0	77.8	141.7
NGC 1300	37.2	37.8	38.8	37.5	38.1	38.8	12.5	24.4	65.6	5.8	11.7	34.0	4.3	11.2	34.0	4.7	14.4	24.5	58.8	75.6	121.7
NGC 1365	37.2	38.2	40.1	37.6	38.5	40.1	12.9	40.0	153.5	5.8	19.6	71.9	4.3	19.4	72.1	8.3	22.0	35.1	77.3	96.4	183.4
NGC 1385	37.3	38.3	39.3	37.8	38.5	39.4	16.6	45.7	120.9	8.0	23.4	55.6	7.0	23.4	55.4	8.7	21.6	34.1	49.6	84.8	149.9
NGC 1433	37.0	37.7	38.7	37.3	37.9	38.7	10.5	24.5	61.6	4.9	12.0	31.9	4.3	11.8	31.8	6.2	13.8	21.7	58.5	73.5	124.8
NGC 1512	36.9	37.7	39.0	37.4	38.0	39.1	11.3	25.4	102.5	5.0	11.9	51.5	3.5	11.1	51.4	5.4	16.2	24.4	79.1	85.6	177.4
NGC 1566	37.2	38.0	39.1	37.6	38.4	39.2	14.2	35.1	103.6	6.7	17.2	47.8	5.5	16.9	47.8	7.4	17.3	27.9	50.3	86.3	144.3
NGC 1672	37.2	38.1	39.3	37.7	38.3	39.4	14.3	39.6	112.5	6.4	19.6	53.5	5.6	19.6	54.5	8.3	18.5	32.1	63.9	87.2	162.9
NGC 2835	37.0	37.7	38.5	37.4	38.0	38.7	12.1	27.2	64.5	5.7	13.0	32.2	4.2	12.6	32.0	5.3	12.4	23.8	49.1	79.8	119.8
NGC 3351	37.0	37.6	39.0	37.2	37.9	39.1	9.9	19.2	76.7	4.6	10.1	36.2	3.7	9.5	36.7	4.4	8.6	13.1	38.6	65.8	104.1
NGC 3627	37.4	38.3	39.4	37.8	38.6	39.4	15.0	45.2	108.1	7.5	23.7	50.2	7.1	23.7	50.3	10.2	19.1	27.4	49.5	81.9	132.8
NGC 4254	37.4	38.2	39.0	37.7	38.4	39.0	15.2	38.7	81.5	7.3	20.3	40.9	6.2	20.0	40.7	8.6	16.4	25.7	47.5	75.2	120.5
NGC 4303	37.3	38.2	39.1	37.7	38.5	39.3	14.2	38.4	100.5	6.8	18.6	47.1	5.5	18.2	47.1	8.6	16.8	28.1	48.3	84.2	145.4
NGC 4321	37.2	38.0	39.1	37.7	38.3	39.2	13.0	29.6	85.6	5.8	13.2	41.6	5.2	13.2	41.7	5.2	13.8	23.3	60.6	79.4	137.3
NGC 4535	37.2	37.8	38.7	37.5	38.1	38.8	13.1	27.3	63.2	6.3	13.9	30.1	4.9	13.4	29.8	6.2	15.3	21.2	43.4	67.7	112.6
NGC 5068	37.1	37.6	38.1	37.3	37.8	38.2	11.4	24.8	41.0	5.0	12.7	20.3	4.0	12.5	20.1	5.1	11.1	18.4	36.6	49.8	73.0
NGC 7496	37.1	38.1	39.0	37.4	38.2	39.0	13.0	37.3	95.5	6.3	16.7	44.9	4.8	16.2	46.1	7.3	19.2	27.2	57.0	89.3	145.5
All	37.2	38.0	39.1	37.6	38.3	39.1	13.3	33.1	93.8	6.2	16.4	44.2	5.1	16.3	44.4	7.1	16.6	28.3	50.3	79.4	136.7

Notes. We report percentiles (10%, 50%, 90%) for the Hα luminosities measured with HST and MUSE, as well as for several size definitions: circularised radius (r_{circ}, HST), moment-based radius (r_{mom}, HST), deconvolved moment-based radius ($r_{mom,deconv}$, HST), Stromgren radius (r_{str}, HST), and circularised radius from MUSE ($r_{circ,\ MUSE}$). Note that the values for the MUSE sample differ from those in Groves et al. (2023), as here we restrict to the sub-sample also detected with HST in each galaxy (see Table 1).

Table H.2. Distribution of electron densities (n_e) and ionizing photon production rates (Q) for H II regions in each galaxy.

Galaxy	n_e [cm^{-3}]			Q [log(s^{-1})]		
	10%	50%	90%	10%	50%	90%
IC 5332	25.0	38.8	71.9	48.7	49.3	49.9
NGC 0628	19.7	38.8	78.2	48.9	49.5	50.3
NGC 1087	15.9	29.2	52.7	49.1	49.8	50.8
NGC 1300	26.7	40.5	94.6	49.1	49.6	50.5
NGC 1365	25.6	42.3	163.5	49.2	50.1	51.6
NGC 1385	20.5	31.8	57.0	49.2	50.1	51.2
NGC 1433	25.1	45.2	84.8	48.9	49.5	50.4
NGC 1512	22.1	57.6	98.3	48.8	49.6	50.8
NGC 1566	25.6	42.3	83.2	49.2	50.0	51.0
NGC 1672	21.5	40.5	157.5	49.1	50.0	51.2
NGC 2835	19.7	31.8	67.0	48.9	49.6	50.4
NGC 3351	42.3	76.5	249.5	48.9	49.4	50.9
NGC 3627	24.0	45.2	91.1	49.4	50.2	51.2
NGC 4254	24.0	40.5	85.3	49.2	50.1	50.8
NGC 4303	24.0	40.5	79.9	49.2	50.0	51.0
NGC 4321	31.8	55.1	122.1	49.1	49.9	50.9
NGC 4535	27.9	50.4	103.9	49.0	49.8	50.6
NGC 5068	15.5	25.6	63.1	49.0	49.5	50.0
NGC 7496	24.0	37.1	70.1	49.0	49.9	50.8
All	22.4	40.5	87.2	49.1	49.9	50.9

Notes. We report the 10%, 50%, and 90% percentile values.

Table H.3. Distribution of the age and masses of (NUV, 32 pc scale) stellar associations across the galaxies within H II regions only (see Sect. 3.6 for details).

Galaxy	Age [Myr]			Mass [$\log_{10}(M_\odot)$]		
	10%	50%	90%	10%	50%	90%
IC 5332	1.0	1.0	4.6	3.04	3.63	4.21
NGC 0628	1.0	2.0	8.4	3.20	3.86	4.61
NGC 1087	1.0	2.0	8.0	3.48	4.14	4.92
NGC 1300	1.0	4.0	6.2	3.31	3.93	4.55
NGC 1365	1.0	3.0	7.5	3.62	4.37	5.36
NGC 1385	1.0	4.0	8.0	3.48	4.21	5.02
NGC 1433	1.0	1.0	6.0	3.08	4.04	4.58
NGC 1512	1.0	1.0	7.6	3.43	4.05	4.82
NGC 1566	1.0	2.0	7.0	3.63	4.19	5.09
NGC 1672	1.0	3.0	5.0	3.52	4.31	5.15
NGC 2835	1.0	2.0	8.0	3.18	3.97	4.68
NGC 3351	1.0	3.0	7.0	3.27	4.01	5.44
NGC 3627	1.0	4.0	7.9	3.70	4.42	5.21
NGC 4254	1.0	4.0	7.0	3.59	4.34	5.11
NGC 4303	1.0	3.0	7.0	3.58	4.32	5.16
NGC 4321	1.0	3.0	7.0	3.59	4.29	5.14
NGC 4535	1.0	4.0	8.0	3.53	4.18	5.04
NGC 5068	1.0	7.0	10.0	3.10	3.81	4.68
NGC 7496	1.0	1.0	5.2	3.52	4.04	4.88
All	1.0	3.0	7.0	3.49	4.22	5.05

Notes. We report the 10%, 50%, and 90% percentile values.